J. Fluid Mech. (2001), *vol.* 446, *pp.* 271–308.
DOI: 10.1017/S0022112001005766 Printed in the United Kingdom

The reduction and elimination of a closed separation region by free-stream turbulence

By M. KALTER AND H. H. FERNHOLZ
Hermann-Föttinger Institut für Strömungsmechanik, Technische Universität Berlin, Germany

(Received 21 September 1999 and in revised form 9 April 2001)

This paper is an extension of an experimental investigation by Alving & Fernholz (1996). In the present experiments the effects of free-stream turbulence were investigated on a boundary layer with an adverse pressure gradient and a closed reverse-flow region. By adding free-stream turbulence the mean reverse-flow region was shortened or completely eliminated and this was used to control the size of the separation bubble. The turbulence intensity was varied between 0.2% and 6% using upstream grids while the turbulence length scale was on the order of the boundary layer thickness. Mean and fluctuating velocities as well as spectra were measured by means of hot-wire and laser-Doppler anemometry and wall shear stress by wall pulsed-wire and wall hot-wire probes.

Free-stream turbulence had a small effect on the boundary layer in the mild adverse-pressure-gradient region but in the vicinity of separation and along the reverse-flow region mean velocity profiles, skin friction and turbulence structure were strongly affected. Downstream of the mean or instantaneous reverse-flow regions highly disturbed boundary layers developed in a nominally zero pressure gradient and converged to a similar turbulence structure in all three cases at the end of the test section. This state was, however, still very different from that in a canonical boundary layer.

1. Introduction

There have been many studies of the interaction between a laminar or turbulent boundary layer and an external flow which has turbulence but no significant mean shear. These investigations were concerned mainly with zero-pressure-gradient (ZPG) boundary layers and nearly isotropic free-stream turbulence (FST). For a survey the reader is referred, for example, to Hancock (1980), Blair (1983), Castro (1984) and Hancock & Bradshaw (1989). There are many fewer papers if the pressure gradient in the streamwise direction is positive and for which the flow separates and reattaches downstream. Here one finds investigations of the effect of FST on mild adverse pressure gradients (APG) (Hoffmann & Kassir 1988), diffuser performance (Hoffmann 1981), on separation bubbles (Hillier & Cherry 1981; Kiya & Sasaki 1983), on the reattachment process over a backward facing step (Isomoto & Honami 1989) and a normal flat plate followed by a splitter plate (Castro & Haque 1988; Castro 1990). Reverse flow in the mean can even be eliminated completely by FST if the reverse flow is 'weak' (Fernholz 1994; Kalter & Fernholz 1995) although a certain amount of instantaneous reverse flow may remain. Weak reverse flow is characterized by small values of the mean wall shear stress, in contrast to strong reverse-flow regions downstream of e.g. step changes in surface geometry where the skin friction approaches values as high as those in a ZPG boundary layer. In all these

configurations – except for the diffuser – separation was fixed either by the leading edge of the blunt flat plate or the edge of the step or the fence. The latter two configurations generate strong reverse-flow regions. It is well known that the extent of such a strong reverse-flow region can be substantially reduced by FST (Hillier & Cherry 1981 by 44%; Castro 1990 by 32%) but the reverse-flow region cannot be eliminated in these sharp-edged separations.

Not only reduction but also elimination can be achieved, however, if the reverse flow is 'weak', as in a smooth wall separation bubble on a wing or in a diffuser. Since relatively small amounts of FST ($< 6\%$) can change the shape of the mean velocity profile so that the wall shear stress increases, regions of weak reverse flow are especially susceptible to FST and can revert to forward-flow regions. So the small increase in skin friction due to FST observed in ZPG boundary layers (e.g. Hancock 1980; Hancock & Bradshaw 1983; Blair 1983) has potentially a much greater useful effect in weak reverse-flow regions. The reduction or elimination of weak reverse-flow regions on the blades of a radial turbomachine in one of our wind tunnels has not only reduced flow losses and the noise level but also low-frequency oscillations in the tunnel.

Studies on boundary layer separation are often plagued by unwanted three-dimensional effects. These were largely avoided here by generating an axisymmetric boundary layer which approached separation fairly uniformly (see also Alving & Fernholz 1996, hereinafter referred to as AF; Kalter 2001), resulted in a closed reverse-flow region, and developed downstream in a nominally zero pressure gradient until the end of the test section. The length of the separation bubble could be varied between zero and 390 mm. In this paper results are presented for a flow with a closed reverse-flow region having a length of $\Delta x_R = 217$ mm between mean separation and mean reattachment when the free-stream turbulence level ($Tu_\delta = 0.2\%$) was low (LFST). The locations of separation and reattachment are characterized by zero mean skin friction. This wall-bounded shear flow was investigated under medium (MFST) and high (HFST) free-stream turbulence, with Tu_δ being nominally 3.4% and 5.6%, respectively, at the upstream station $x = -5$ mm in the test section (see figure 1). Integral length scales were smaller than the thickness of the boundary layer ($1.15 \geqslant L_x/\delta \geqslant 0.42$, $0.45 \geqslant L_y/\delta \geqslant 0.15$, see Kalter 2001 for details).

The size of the unperturbed separation bubble was chosen according to two criteria: it should be long enough to show that MFST could reduce the bubble length (here to $\Delta x_R = 108$ mm) and that HFST could eliminate the mean reverse flow although a certain amount of instantaneous reverse flow remained; and the bubble should be short and shallow enough to allow as much development of the boundary layer downstream of reattachment as possible for the given test section. AF had found that a boundary layer downstream of a closed reverse-flow region undergoes a relaxation process which is different from that described by Smits & Wood (1985) so that it is of interest to investigate the reaction of the boundary layer to the strength of the bubble by varying its length, and to the character of the reverse flow, whether considering mean or instantaneous values.

It should be mentioned here that the flow configuration with low free-stream turbulence is similar to the flow investigated earlier by Driver (1991), AF and Na & Moin (1998). With reference to the AF experiment, which was performed in the same wind tunnel, the present test cylinder was elongated in the upstream direction so that transition occurred before the start of the adverse pressure gradient.

Reynolds number effects, as observed in low Reynolds number boundary layers ($Re_{\delta_2} \leqslant 2000$) with FST by Castro (1984), are most likely insignificant in the present flow since the Reynolds number rapidly rises beyond 2×10^3 due to the APG.

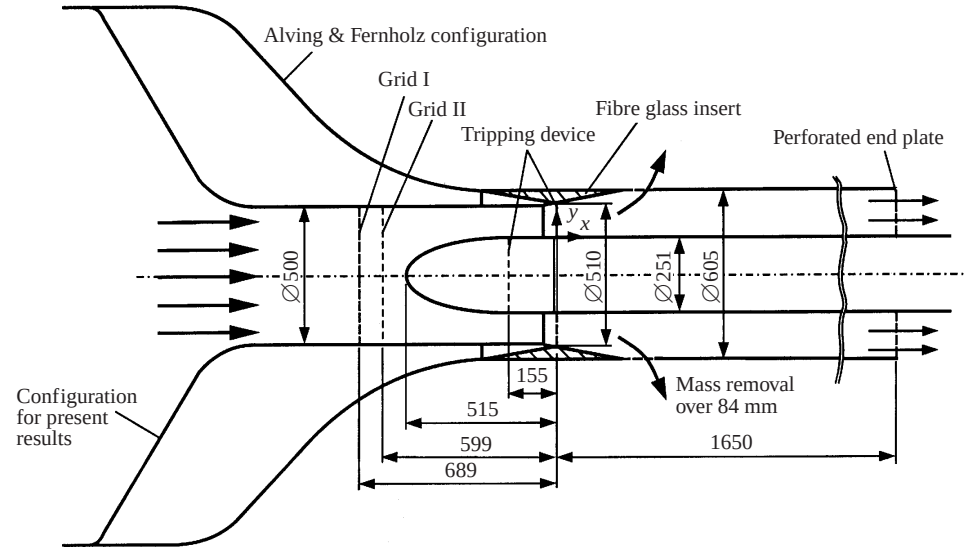

FIGURE 1. Sketch of the test section.

For two reasons it has been important to use laser-Doppler anemometry (LDA) for the measurement of mean and fluctuating velocity components in and above the reverse-flow region. First, instantaneous reverse flow extended to relatively large distances normal to the wall and at least one bubble length downstream from reattachment near the wall and, secondly, the local turbulence level was very high (up to 300%). Both effects would have made hot-wire measurements invalid.

Previous measurements by Kalter (cases A and B, not shown here) were used for the validation of Reynolds stress models by Schatz, Rung & Thiele (1998). For a discussion of boundary layer velocity profiles at and near APG-induced separation the reader is referred to Dengel & Fernholz (1990) (here referred to as DF) and to AF and Alving & Fernholz (1996).

In the following, we describe the experimental arrangement and the measuring techniques in § 2, free-stream turbulence and mean flow behaviour in § 3 and flow properties in the reverse-flow region with and without FST manipulation in § 4. A discussion of the effects of the free-stream turbulence on the separation bubble and the development of the wall-bounded shear layer downstream is finally presented in § 5.

2. Experimental arrangement and measuring techniques

The wind tunnel was the same open-return blower facility described in DF. Air entered, however, through a box filter of a much higher filter quality than that of the former non-woven filter mat, passed through a 12 kW centrifugal fan, and entered a settling chamber with circular cross-section 2000 mm long and approximately 2000 mm in diameter. At the upstream end was a single, precisely manufactured, perforated metal plate (64% porosity) and a non-woven filter mat to improve the flow uniformity. The fan speed was controlled within ± 1 r.p.m. and guaranteed a constant unit Reynolds number of $1.175 \times 10^6\,\mathrm{m}^{-1}$. The throat velocity was approximately $18.0\,\mathrm{m\,s}^{-1}$.

The test section used in this experiment is shown in figure 1 and is similar to that described in AF, with some smaller modifications as discussed below. The hollow

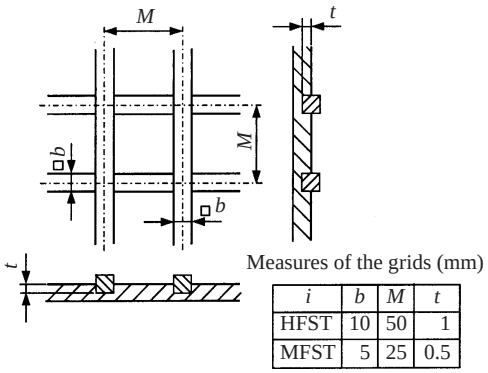

Measures of the grids (mm)

i	b	M	t
HFST	10	50	1
MFST	5	25	0.5

FIGURE 2. Turbulence grid.

aluminium circular cylinder, 1650 mm in length and 251 mm in diameter, which formed the test surface was elongated in the upstream direction by a section of the same diameter, 155 mm in length, so that the boundary layer could be tripped upstream of the start of the APG region at the nosecone/cylinder junction. The tripping device was a Velcro-tape, 2.6 mm in height and the elliptical nose cone had a length of 360 mm. The test surface was surrounded by a concentric, perforated cylinder forming the outer wall (diameter 605 mm) and ended at a perforated end plate.

In order to keep the external grid-generated turbulence nearly isotropic, the contraction of the wind tunnel had to be modified. A new short contraction was inserted feeding a constant-area circular duct of length 1050 mm and internal diameter 500 mm. This in turn is faired into a fibreglass insert which diverges at 10° before meeting the original interior surface 250 mm downstream, with a diameter of 605 mm. The contraction ratio from the settling chamber to the duct is 16.0 and due to the presence of the inner cylinder (contraction ratio of 1.34) results in a total of 21.4. The mean velocity distribution at the inlet of the test section was uniform to within 0.3% and the turbulence intensity $(\overline{u'^2})^{1/2}/u_{\text{throat}}$ was 0.2% (between 0.1 Hz and 50 kHz).

The streamwise pressure gradient was tailored to generate the separation bubble. The location and the size of the closed reverse-flow region were determined by the flared insert, the degree of the perforation of the end plate (53%) and by the length of the perforated region of the outer cylinder wall (38%) just downstream of the flare. In the present case the perforated area was 84 mm long while the remainder of the cylinder was covered with self-adhesive plastic sheeting. The boundary layer downstream of the trip at $x = -155$ mm is turbulent.

Provision was made in the circular duct for mounting square-mesh square-bar biplane grids, following Hancock 1980, intended to produce near-isotropic turbulence. The dimensions of the two grids for medium free-stream turbulence (MFST) and for high free-stream turbulence (HFST), are given in figure 2.

The data were obtained using a microcomputer system with A to D converters, D to A converters, and an IEEE-card to control peripheral devices like digital voltmeters. Temperature measurements were made using a temperature sensor and a digital voltmeter. Another digital voltmeter was used to read the output voltage of the pressure transducer and a FV-manometer. The pulsed-wire anemometer was controlled using a parallel port card on the VME-bus. Hot-wire signals were digitized using a 12-bit analogue-to-digital converter card. Data acquisition was achieved using Rhotron hardware controlled by an Atari microcomputer.

The streamwise static pressure was measured using a single movable tap (see AF). This static tap (as well as all wall probes) was mounted into a plug which fitted into a streamwise slot of 20 mm width milled along the length of the test surface. As a refinement over the DF test cylinder, the surface of these interchangeable plugs had the same transverse radius of curvature as the rest of the cylinder, to remove the possibility of flat plug surfaces affecting wall measurements. Static pressure was referenced to that at the throat, measured with a Pitot-static tube in the free stream located $\approx 160^\circ$ around the circumference from the measuring position.

The free-stream velocity was monitored by the Pitot-static tube mounted near the entrance of the test section at a position $x = 6$ mm, i.e. 161 mm downstream of the tripping device and $y \approx 65$ mm above the cylinder.

For measurements of static pressure and small pressure differences of Pitot-static tubes, Preston tubes and static pressure taps, a *MKS Baratron 220C* differential pressure transducer with a range of 100 Pa was used. This gauge was temperature stabilized and calibrated for both positive and negative pressure differences. The accuracy is 0.15% of the reading. The output voltage of the transducers was measured with a digital voltmeter type HP-34401A.

The streamwise component of the fluctuating wall shear stress was measured with two wall-mounted pulsed-wire probes (Bradbury & Castro 1971; Castro 1992) as well as with a wall hot-wire probe calibrated in ZPG against a Preston tube. Both methods are described in a recent review by Fernholz *et al.* (1996). Far upstream and downstream of separation wall hot-wire probes were used. The wall pulsed-wire probes were each integrated into one of the interchangeable plugs described above and the wires were 0.05 mm above the wall. The probe with the more closely spaced wires ($\Delta l = 0.5$ mm) was used in and around the separation bubble (344 mm $\leqslant x \leqslant$ 561 mm), while the one with wires spaced farther apart ($\Delta l = 0.7$ mm) was used elsewhere. Both, the wall-mounted pulsed-wire probes and the LDA measured the probability of reverse flow, χ, which is defined as the ratio of samples indicating flow in the upstream direction to the total number of samples.

The absolute values of the wall shear stress can be very low in regions where the flow separates or reattaches. Therefore, the sensors were modified in order to increase their sensitivity (at the cost of losing spacial resolution). After some experiments, a sensor was chosen that had a pulser wire with a diameter of 5 μm and a length of 5.0 mm. It was positioned 0.05 mm above the wall. The sensor wires had a diameter of 2.5 μm and an active length of 2.5 mm. Based on the maximum wall shear stress in the reverse-flow region downstream of the fence, the length of the sensor wires in wall units was $l^+ = l\,u_{\tau_{max}}/\nu = 67$. A sampling frequency of 25 Hz was used for all measurements, up to 20 000 (dependent on the time to get reproducible values for the higher moments) samples were taken at every position, resulting in a sampling time of about 5 to 13 minutes.

The three components of the fluctuating velocity and one-dimensional power spectral densities were measured using single and X-wire probes wherever possible. The X-wire probes had a cage face of 1.5 mm × 0.5 mm in case of the UV-probes and 1.5 mm × 0.3 mm in case of the UW-probes (see Dengel 1992). LDA was used in regions where reverse flow occurred or, where the turbulence intensity was high.

The hot-wire anemometer was an IFA-100 constant-temperature anemometer (square-wave-test response in excess of 40 kHz). The pulsed-wire anemometer was built in-house (Wagner 1986). The probes were traversed away from the wall using an electrically driven mechanism (built on a plug fitting into the above described slot)

with an incremental resolution of 0.005 mm. Probe access was through a slot in the wall of the outer cylinder.

The two-component laser-Doppler anemometer (*Dantec*) used for velocity measurements operated in backscatter mode. It consisted of two *Dantec* burst-spectrum analyser (BSA) modules (type 57N10 master and 57N25 slave), a *2d-Fiberflow* probe with a focal length of 600 mm, a *Dantec* transmitter box with four fibre manipulators and a 300 mW argon-ion laser. The BSA units were operated in continuous mode in order to minimize errors due to velocity bias (for a detailed listing of the parameter settings used here and a discussion of possible errors together with a comparison of LDA- and hot-wire measurements the reader is referred to Kalter 2001). It should be mentioned, however, that some hot-wire measurements were performed in regions with high levels of turbulence where the usual correction procedures cease to apply. In these cases and, if instantaneous reverse flow occurred, we have used the LDA-data wherever they were available.

The measuring volume was an ellipsoid with axes of 1.4 mm and of 88 μm. In order to make measurements in the vicinity of the wall, the probe was inclined by an angle of approximately 6° towards the horizontal plane. For the LDA measurements panes of protective glass from a welding mask were built into plugs fitting into the slot described above. This material reflects laser light well when the measuring volume is close to the wall. The distance normal to the wall could be adjusted to an accuracy of 50 μm and the probe holder was traversed using a two-dimensional traverse (type *Isel*). Measurements were monitored using a *Krenz DSO 3350* oscilloscope. The data acquisition was controlled by a 486 personal computer using the *Dantec* software *BurstWare 3.11*.

The flow was seeded by means of a *Pallas AGF 10* cyclone seeder which created a fine mist of diethylhexylsebacat (DEHS) which was introduced at the inlet of the wind tunnel.

3. Experimental results: free-stream turbulence and mean flow behaviour

Figure 3(*a*) presents the development of the free-stream fluctuating velocities u'_{rms}, v'_{rms} and w'_{rms} for the case of HFST. u'_{rms} is shown as the turbulence intensity $Tu_{\delta_{ref}} = (\overline{u'^2})^{1/2}_{\delta}/u_{\delta_{ref}}$ (LFST and HFST). Figure 3(*b*) presents $Tu_{\delta} = (\overline{u'^2})^{1/2}_{\delta}/u_{\delta}$ (for HFST only), with u_{δ} as the mean velocity at the edge of the boundary layer ($\delta_{99.5\%}$) and $u_{\delta_{ref}}$ at the reference station $x = -5$ mm. In accordance with Hancock & Bradshaw (1989) the FST values were measured in a region where the intensities cease to vary with y, i.e. approximately in a range $1.1 \leqslant y/\delta \leqslant 2$ (see § 4). The decay of the FST downstream of the grid gave values at $x = -5$ mm in accordance with the decay law given by Baines & Peterson 1951, for example.

The distributions of u'_{rms}, v'_{rms} and w'_{rms} show the typical decay in the downstream direction despite the APG in the upstream part of the test section (not shown here, see Kalter 2001).

The measured ratios of the lateral r.m.s. intensities w' and v' and the streamwise intensity are within 5% of u' at the upstream end of the flow – usual for good-quality grid-generated turbulence (Hancock & Bradshaw 1983) – and then decrease to less than 80% of the value of u', followed by a small increase to a plateau with levels between 80% and 85%.

The behaviour of Tu_{δ} is caused by the fall of u_{δ} in the APG-region for MFST (not shown) and HFST leading to peak values of 5.6% and 7.8%, respectively. For the

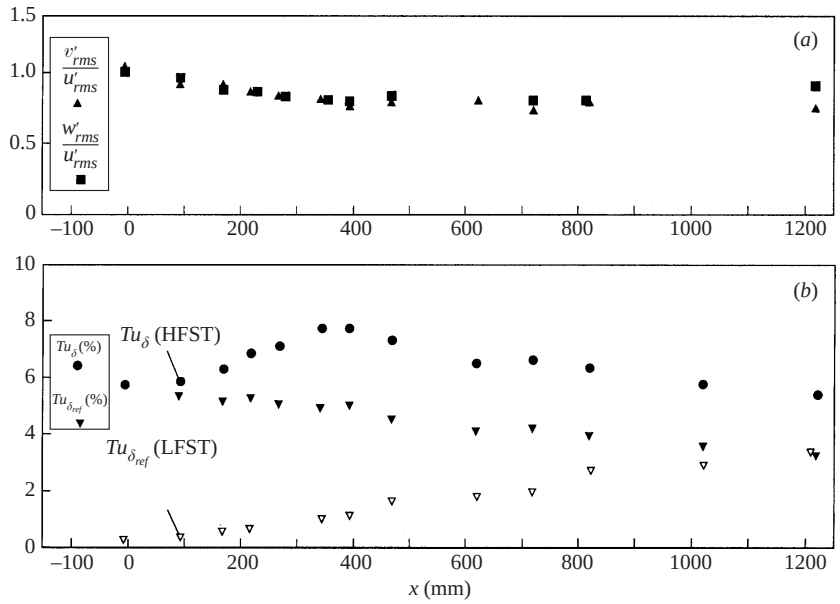

FIGURE 3. Streamwise distributions of (*a*) the isotropy parameters $(w'/u')_\delta, (v'/u')_\delta$ and of (*b*) the turbulence intensities $Tu'_\delta, Tu'_{\delta_{ref}}$ for HFST (hot-wire data, $\bar{u}_{\delta_{ref}} = 17.9\,\mathrm{m\,s^{-1}}$).

LFST case we note a continuous increase in the x-direction due to the strong effects of the separation region (Tu_δ begins to rise near separation) and its downstream effects on the outer flow region of the boundary layer. This effect is further increased by the convergence of the outer – and inner – cylinder boundary layers and the final annihilation of the 'potential core'.

Hancock & Bradshaw (1983) defined as a length scale of free-stream turbulence a form of dissipation length parameter L^u_e according to the equation

$$u_\delta \frac{\mathrm{d}(\overline{u'^2})_\delta}{\mathrm{d}x} = -\frac{(\overline{u'^2})^{3/2}_\delta}{L^u_e}\,, \tag{3.1}$$

where x is measured from the grid position. In their experiments $L^u_e/\delta_{99.5\%}$ varied between 5 and 0.67 and in the present HFST case between 2.83 and 0.85. Since it is not clear whether this relationship holds also for flows with variable pressure gradients we have determined integral length scales in the streamwise (x) and wall normal (y) directions. The former was calculated from the autocorrelation of u', using Taylor's hypothesis, and the latter from a space correlation of u'. The distributions of L^u_x and L^u_y in the streamwise direction were made dimensionless by the boundary layer thickness $\delta_{99.5\%}$ at $x = -5\,\mathrm{mm}$ (δ_{ref}). Although the integral length scales increase approximately by a factor of 3 along the test section (figure 4), they remain of the order of the boundary layer thickness at the reference station ($x = -5\,\mathrm{mm}$). L^u_x is a mean value of length scales measured in a range up to 3δ outside the boundary layer. L^u_y is the length scale determined with the fixed probe at the edge of the boundary layer.

Figure 4 shows the ratios L^u_x/δ_{ref} and L^u_y/δ_{ref} for medium and high free-stream turbulence with the main result that the former varies between 1.2 and 3.2 and the latter between 0.45 and 1.1 giving approximately a ratio of 3 for L^u_x/L^u_y.

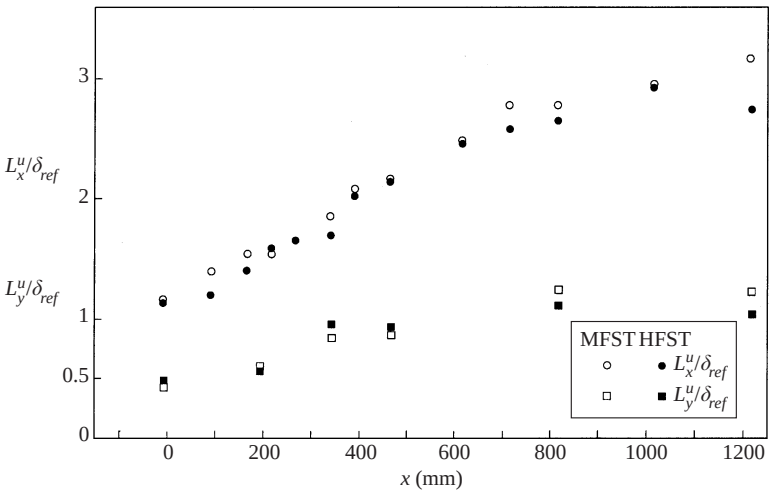

FIGURE 4. Streamwise distributions of the integral length scales L_x^u/δ_{ref} and L_y^u/δ_{ref}.

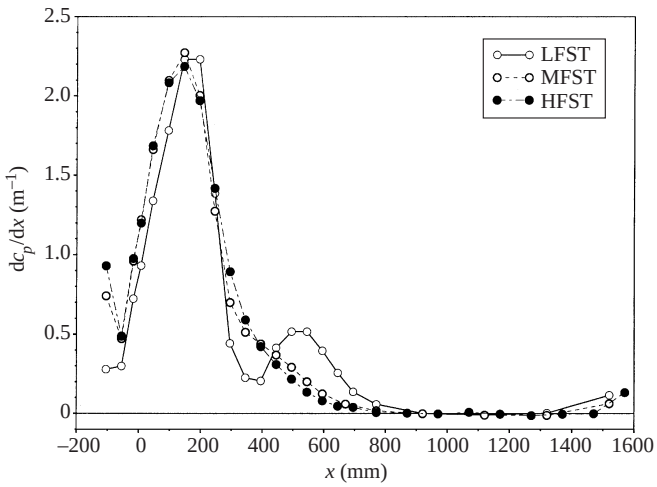

FIGURE 5. Streamwise distributions of the pressure gradient dp/dx for LFST, MFST and HFST.

If the length scales are made dimensionless by the local boundary layer thickness (see Kalter 2001), $L_x^u/\delta_{99.5\%}$ and $L_y^u/\delta_{99.5\%}$ vary in the streamwise direction between 1.15 and 0.42 and 0.45 and 0.15, respectively, with little difference between cases MFST and HFST. Spectra which were made dimensionless by L_x^u are discussed in § 4.

The respective static pressure gradients in the streamwise direction which are the governing boundary conditions for the boundary layers are presented in figure 5. They show a strong increase with little difference in the peak value and then reach zero in the relaxation region. The case with LFST develops a second but much smaller peak in the reattachment region which can be explained by the smaller displacement of the flow downstream of the bubble.

It is appropriate to begin the discussion of the mean flow with the streamwise distributions of the static pressure coefficient c_p, the skin friction coefficient c_f, and

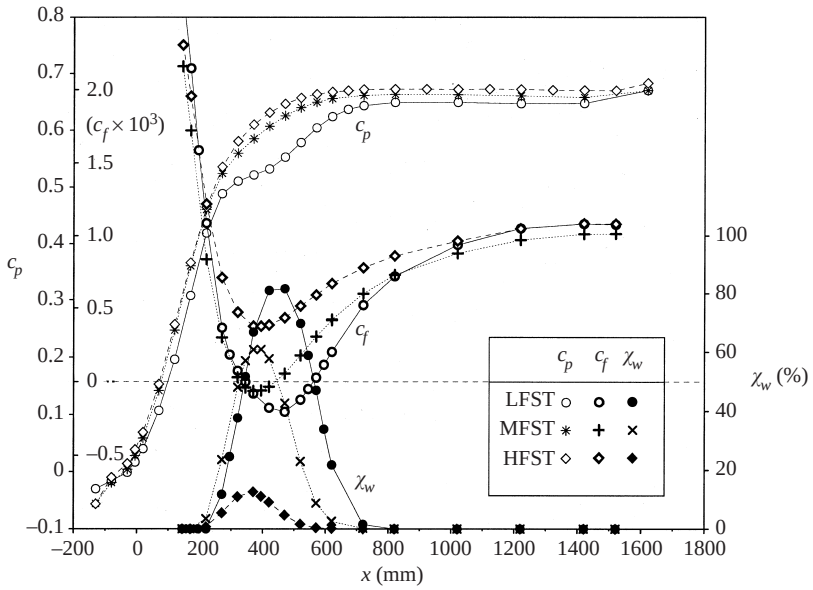

FIGURE 6. Streamwise distributions of the wall parameters: static pressure coefficient c_p, skin-friction coefficient c_f, and reverse-flow parameter χ_w.

the reverse-flow coefficient at the wall χ_w

$$c_p(x) = \frac{p(x) - p_D}{\frac{1}{2}\rho u_D^2}, \tag{3.2}$$

$$c_f(x) = \frac{\overline{\tau}_w(x)}{\frac{1}{2}\rho u_D^2}, \tag{3.3}$$

$$\chi_w(x) = \chi(x, y)|_{y=0}, \tag{3.4}$$

where $p(x)$ is the wall static pressure, $\overline{\tau}_w(x)$ the mean wall shear stress, ρ the density, p_D and u_D the pressure and velocity at the location of the reference Pitot-static tube and $\chi(x, y)$ the probability of the reverse flow at any point. Figure 6 presents the curves for the three cases LFST, MFST, and HFST, respectively. Skin friction was measured by means of a wall hot wire and a wall pulsed wire in cases where reverse flow occurred.

LFST shows the typical c_p-distributions for a flow with a separation bubble. Mean separation ($x_S = 344\,\text{mm}$) and reattachment ($x_R = 561\,\text{mm}$) define a mean bubble length of $\Delta x_R = 217\,\text{mm}$ and are characterized as the locations where $c_f = 0$ and $\chi_W = 50\%$ (see also AF; Ruderich & Fernholz 1986). The length of the 'shoulder' in the pressure distribution corresponds roughly with the length of the bubble. The upstream c_p and c_f distributions are nearly identical for all three cases, showing the dominant effect of the pressure gradient until instantaneous reverse flow occurs at the wall, with χ_w increasing from zero. The c_f values for the LFST and MFST flows which will separate are virtually identical until χ_w reaches 50%, i.e. the onset of mean flow separation. They then diverge both from each other and from the mean-flow-attached case HFST which lies higher throughout. With this divergent history it is surprising that all three cases rapidly tend to a common value of c_f (see figure 6) downstream at about 1.1×10^{-3}, within 3% by the c_f distribution of all three cases,

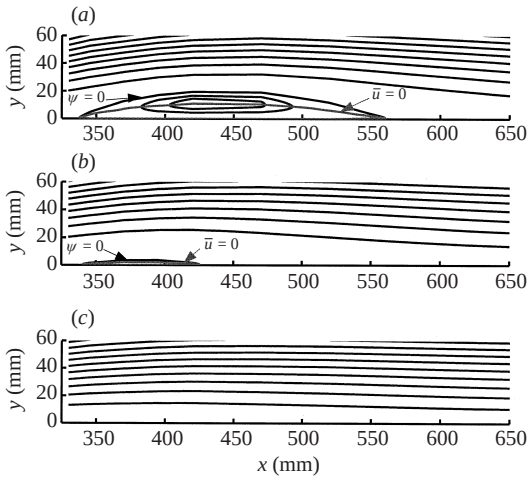

FIGURE 7. Mean streamlines for (*a*) LFST, (*b*) MFST and (*c*) HFST.

	x_S (mm)	x_R (mm)	Δx_R (mm)	$\eta_m = y_{max}(\bar{u}=0)$ (mm)	$\eta_\psi = y_{max}(\psi=0)$ (mm)
LFST	344	561	217	10.9	19.4
MFST	331	439	108	2.0	3.6
HFST	–	–	–	–	–

TABLE 1. Locations of separation, x_S, reattachment, x_R, and the resulting lengths of reverse-flow regions, Δx_R.

while the locally defined quantity $c_{f_{local}} = \bar{\tau}_w/0.5\rho u_\delta^2$ tends to 3×10^{-3}. It is interesting to note that the skin friction is at most only 5% higher than in a canonical boundary layer at the same Reynolds number.

Instantaneous reverse flow was observed for LFST in a region extending from half a bubble length upstream of mean separation to one bubble length downstream of reattachment (see figure 6). This shows the 'buffeting behaviour' of the flow (see also AF; Simpson, Chew & Shivaprasad 1981; Fernholz 1993; Na & Moin 1998). In agreement with the observations of AF the bubble location for LFST and MFST is well defined in the mean, however, and quite repeatable from day to day.

Since the distributions of c_p and $\mathrm{d}c_p/\mathrm{d}x$ are almost identical for MFST and HFST until χ_w departs from zero, it must be the effect of the FST on the mean velocity profiles and the turbulence structure which changes the c_f- and χ_w-distributions when compared to those of case LFST. Although the boundary layer of case MFST still separates, its mean reverse-flow length is reduced by about half to $\Delta x_R = 108\,\mathrm{mm}$ and χ_w to a maximum value of 61% compared with 82% for LFST. For HFST the mean value of c_f is always positive but χ_w has a maximum value of 12.5% indicating that there is still instantaneous reverse flow in the near-wall region.

Mean streamlines with constant ψ for the three cases are shown in figure 7 and the intersections of the mean dividing streamline ($\psi = 0$) with the wall are $x = 337\,\mathrm{mm}$ and 562 mm (cf. the mean separation and reattachment locations in table 1) for LFST.

The extent of the reverse-flow region normal to the wall ($y/\delta \geqslant 0.001$) may also be demonstrated by the profiles of the probability of reverse flow $\chi(y)$ over the bubble.

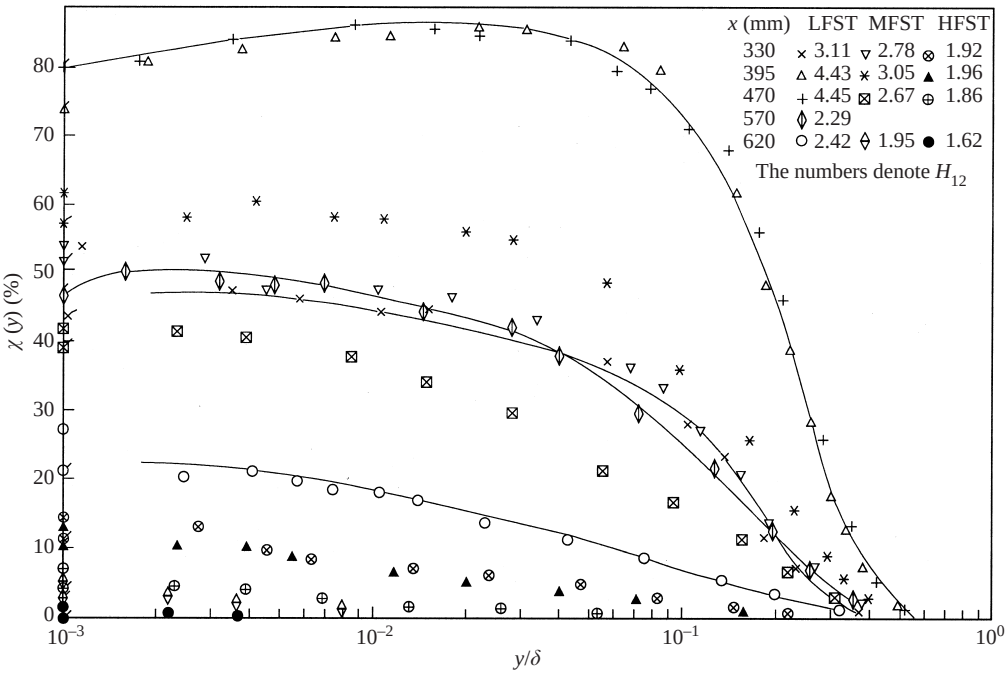

FIGURE 8. Profiles of the probability of reverse flow for LFST, MFST and HFST. Measurements from LDA and wall pulsed-wire probe ($'$). (Lines are for visual aid only.)

Figure 8 presents five χ-profiles for LFST plotted against y/δ on a logarithmic scale in the range 330 mm $\leqslant x \leqslant$ 620 mm. The profiles rise steadily towards the wall but we cannot exclude a maximum close to, rather than at the wall, with a decrease towards the wall value. In the proximity of the wall ($y = 0.05$ mm) there are measurements both by a wall pulsed-wire probe (symbols marked by $'$) and by LDA. The latter data are in general slightly higher but we trust the WPW-data more since there were always 15 000 samples as compared with about 5000 for the LDA in the near-wall region. The profiles show that, when the bubble reaches its greatest height, instantaneous reverse flow extends to 50% of the boundary layer thickness δ and that up to 10% of δ the reverse flow exceeds 75%. The χ-profiles at $x = 330$ mm and $x = 570$ mm are slightly upstream of separation and downstream of reattachment respectively, but agree well, qualitatively, with the profile near separation ($x = 330$ mm) of MFST. This suggests a similar behaviour of the χ-profiles at separation and reattachment as was found for the respective mean velocity profiles (e.g. DF; AF).

Figure 8 shows also the effect of the free-stream turbulence which, for example, reduces the probability of reverse flow to about 12% for HFST compared with that for LFST and confines the reverse flow to a region of about 10% of the boundary layer thickness. This means no mean reverse flow and an almost complete elimination of the reverse-flow region. The effect is less strong for MFST with an upper limit of $\chi = 60\%$ instead of 85% and consequently a shorter and a more shallow bubble (cf. figure 7).

A more general view on the effect of the FST is seen in figure 9. Here the mean velocity profiles, made dimensionless by the reference velocity u_D, are plotted against y for LFST, MFST and HFST in the regions where instantaneous or mean reverse flow

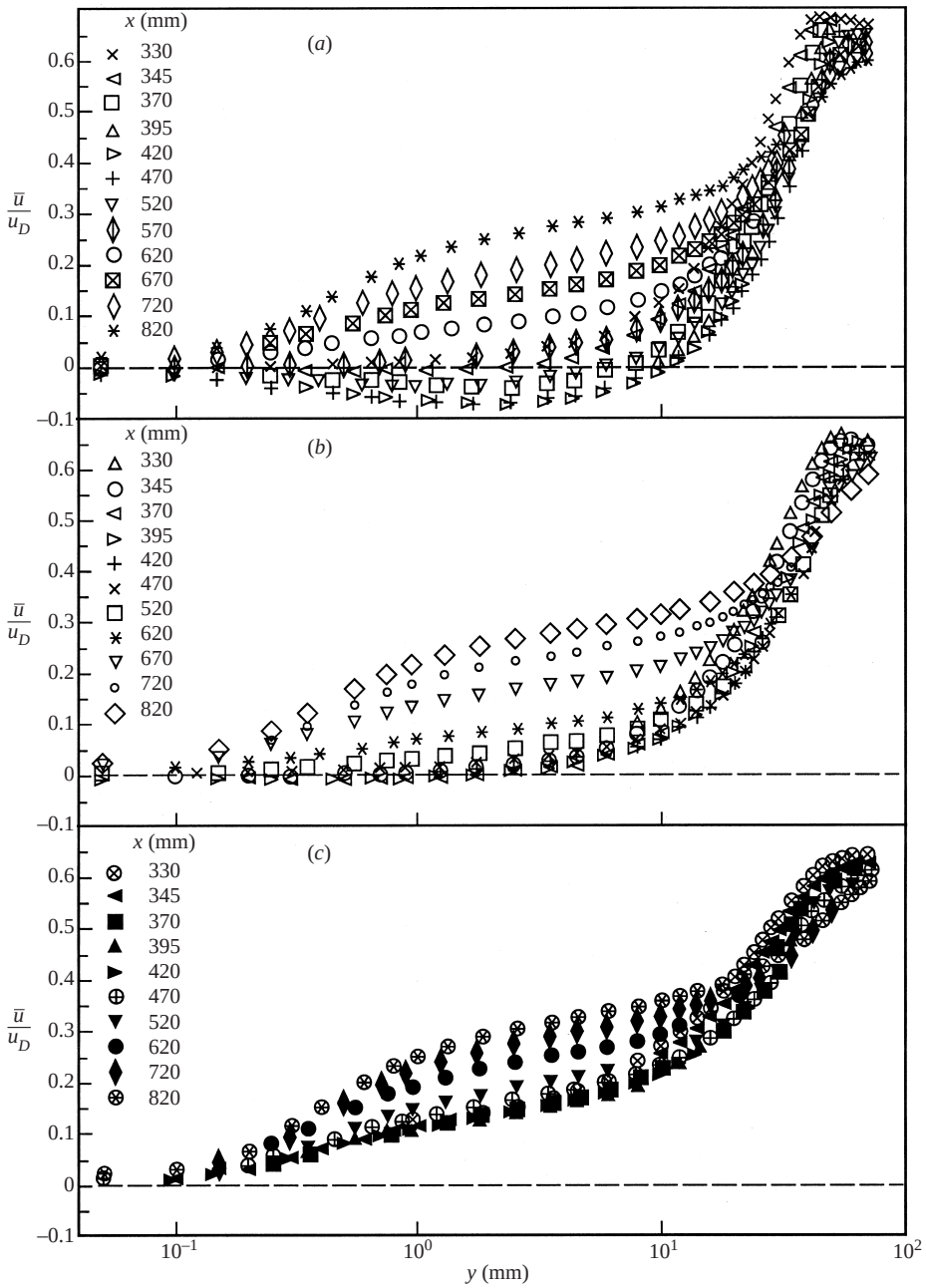

FIGURE 9. Mean velocity profiles for (*a*) LFST, (*b*) MFST and (*c*) HFST in regions with instantaneous or mean reverse flow (LDA-measurements).

occurred (LDA-measurements). Symbols for the profiles and characteristic parameters are given in table 2.

Figure 10 presents the development of the shape parameter H_{12} for the three cases. As found by DF and by AF, separation and reattachment (LFST and MFST) are characterized by values of $H_{12} = 2.85 \pm 0.1$ (remember that $\chi_w \approx 50\%$). The mean reverse-flow region shows values of H_{12} up to 4.6 and Simpson, Strickland &

Symbol	x(mm)	H_{12}	Re_{δ_2}	$c_{f_{loc}}(\times 10^3)$	$Tu_\delta(\%)$	$\chi_w(\%)$	c_p
				LFST			
◇	−5	1.43	1354	3.99	0.23	0	0.017
▨	95	1.45	1871	3.35	0.31	0	0.152
⊘	170	1.57	2665	2.54	0.50	0	0.308
◬	220	1.81	3643	1.56	0.60	0	0.419
◇	270	2.20	4681	0.62	0.60	13.4	0.488
×	330	3.11	5541	0.09	1.44	43.4	0.513
◁	345	3.37	5640	−0.06	1.31	52.4	0.517
□	370	3.99	5481	−0.18	1.73	66.9	0.522
△	395	4.43	5440	−0.29		74.0	0.527
▷	420	4.60	5574	−0.40	1.87	81.1	0.532
+	470	4.44	5789	−0.47	2.14	80.0	0.553
▽	520	3.66	6660	−0.29	2.57	69.8	0.579
◊	570	2.92	7503	0.05	2.84	46.7	0.604
○	620	2.42	8104	0.55	3.13	21.2	0.624
◊	720	1.84	8597	1.50	4.08	1.6	0.644
∗	820	1.58	7969	2.17	2.60	0	0.649
◇	1020	1.36	7971	2.70	2.80	0	0.649
▽	1220	1.29	7675	2.96	3.30	0	0.647
				HFST			
◆	−5	1.38	1963	3.76	5.6	0	0.039
◣	95	1.39	2496	3.46	5.8	0	0.205
◒	170	1.49	2733	2.73	6.2	0	0.366
◭	220	1.60	4566	2.10	6.7	0.7	0.465
◆	270	1.74	5416	1.46	7.1	5.8	0.536
⊗	330	1.92	6394	1.15	8.0	11.2	0.586
◀	345	1.93	6779	1.06	7.8	12.2	0.595
■	370	1.95	7202	1.04	7.9	11.5	0.610
▲	395	1.96	7548	1.01	7.7	10.8	0.621
▶	420	1.94	7929	1.06	7.7	9.0	0.631
⊕	470	1.86	8259	1.23	7.5	4.3	0.646
▼	520	1.78	8598	1.44	7.5	1.6	0.657
●	620	1.60	8954	1.92	6.5	0	0.668
◆	720	1.52	8534	2.19	6.6	0	0.672
⊗	820	1.44	8857	2.51	6.2	0	0.672
◆	1020	1.35	9284	2.67	5.7	0	0.672
▼	1220	1.30	8821	2.86	5.2	0	0.672

TABLE 2. Symbols and characteristic parameters for cases LFST and HFST.

Barr (1977) and Simpson *et al.* (1990) found even higher values in an open reverse-flow region. HFST shows maximum values $H_{12} \approx 2$ for about the same pressure distribution, which is indicative of a much fuller velocity profile due to the FST than in the other two cases. The start and downstream values of the H_{12}-distribution fall on top of each other with a very small effect of the FST.

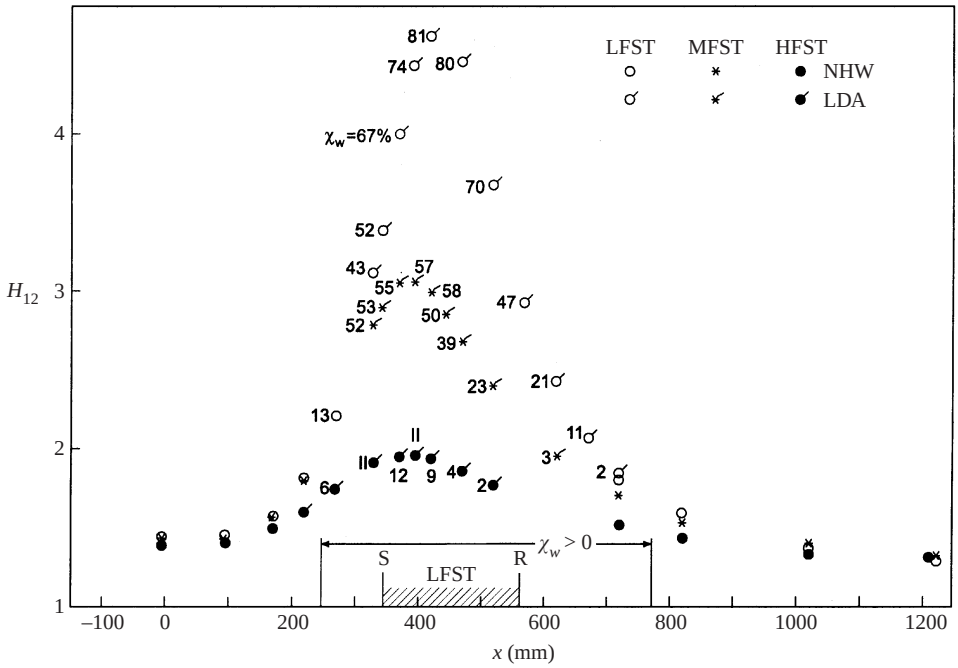

FIGURE 10. Streamwise distributions of the shape parameter H_{12} for the three cases (numbers attached to the symbols denote χ_w, NHW means normal hot wire).

Since the mean wall shear stress was measured by a wall pulsed wire in the region with mean or instantaneous reverse flow and a wall hot wire in the upstream and downstream regions, the velocity data are well suited to check the validity range of the logarithmic law of the wall. The absence of a log law in an APG boundary layer where instantaneous reverse flow occurs (i.e. $\chi_w \neq 0$) is now well established (e.g. Simpson *et al.* 1981; DF) but it is not clear how an APG with FST affects the log law.

Hancock & Bradshaw (1983) claim that in a ZPG flow free-stream turbulence does not influence the validity of the log law up to $Tu_\delta \approx 7\%$, however, with $\overline{\tau}_w$ based on the slopes of the velocity profiles in the semi-log inner region. Preston tube measurements were also made for several cases, using the calibration of Patel (1965), and agreed with the values from the profiles (Hancock & Bradshaw 1983). In the case of discrepancies in the experiments here one could then suppose that it is the APG and not the FST which invalidates the log law.

Figure 11 presents mean velocity profiles in inner-law scaling in the region upstream of separation (with $\chi_w = 0$) for LFST and HFST where Tu_δ varies from 0.2 to 0.6 and 5.6 to 6.7, respectively. The profiles at the first two stations show good agreement with the log law ($\kappa = 0.40$ and $C = 5.10$). Deviations occur at $x = -170$ mm, i.e. in the early adverse pressure region and well ahead of separation. Since we do not know of a satisfactory criterion denoting the breakdown of the validity range of the log law (see the discussion in AF) we have used the ratio of the local maximum Reynolds shear stress to the local wall shear stress $\overline{\tau}_w$ as an indicator (Simpson 1989). This ratio should be smaller than 1.50 for the log law to hold. Here we find 1.34 for LFST and 1.70 for HFST which are close to the above limit.

Downstream of reattachment the profiles again lie first below the log law for LFST and HFST (figure 12), a behaviour typical for the redevelopment region as noted

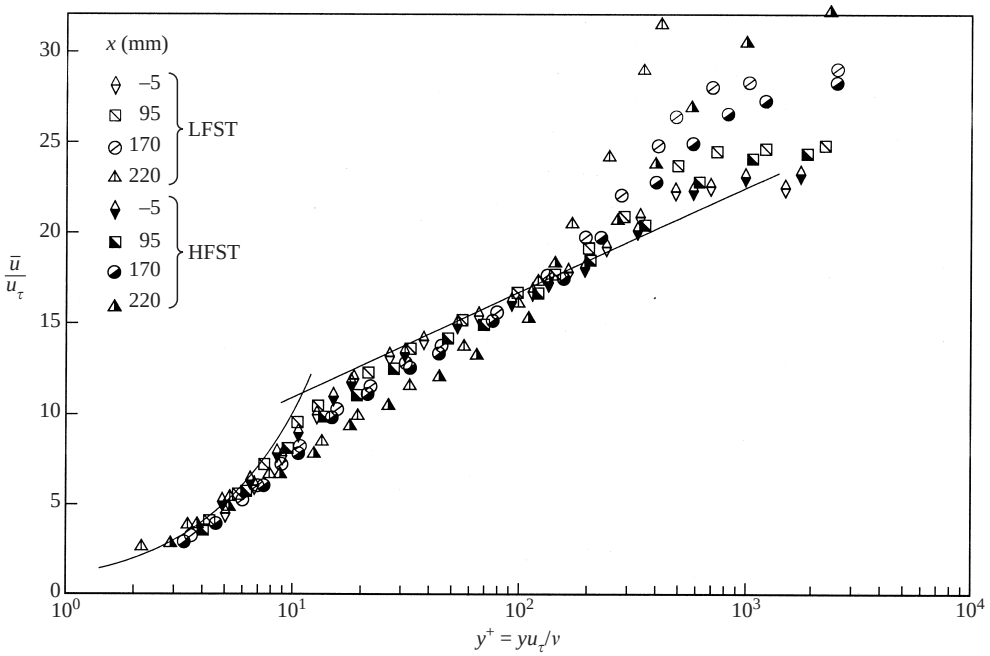

FIGURE 11. Mean velocity profiles in inner-layer scaling in the APG region upstream of separation for LFST and HFST (NHW-data) (for characteristic parameters see table 2).

by Bradshaw & Wong (1972), Ruderich & Fernholz (1986), AF and Castro & Epik (1996), for example. Although the mean skin friction is always positive for the velocity profiles of HFST they lie below the log law as long as there is instantaneous reverse flow in the near-wall region (see Simpson 1981; DF).

The velocity profiles then converge towards the log law but agree with it only after the last measuring station ($x = 1220$ mm) where the pressure gradient is zero and Tu_δ 3.3% and 5.2%, respectively.

This convergence in the two cases shows that the development of the mean velocity profiles in the inner region of the boundary layer is largely independent of FST (see also Castro & Epik 1998) and, even more surprising, independent of the 'new' starting conditions influenced by the reverse-flow region. This is long for LFST, short for MFST and characterized by instantaneous but no mean reverse flow for HFST.

The outer region of the mean velocity profile, in contrast, has not yet recovered at the last measuring station ($3\Delta x_R$ or $10.5\delta_R$ downstream from reattachment, with $\delta_R = \delta_{99.5\%}$ at reattachment) and the wake factor is smaller than it would be in a canonical boundary layer. From this it is inferred that the FST does not strengthen the downstream turbulence structure and this is confirmed by the Reynolds stress profiles which are shown in figure 13. Both the profiles of the Reynolds normal stress $\overline{u'^2}$ and those of the shear stress $\overline{u'v'}$ fall onto each other if made dimensionless by $u_{\tau_{ref}}$ and plotted over y/δ for LFST, MFST and HFST. The comparatively low values at $x = 1220$ mm reflect the unfinished recovery of the near-wall turbulence structure and the apparently weak influence of the FST on the downstream flow.

The different levels of the FST, however, influence the profiles of the Reynolds stresses strongly at the upstream station ($x = -5$ mm), with the normal stress profiles showing a hump in the outer layer (figure 13*a*) and the shear stress profiles reaching

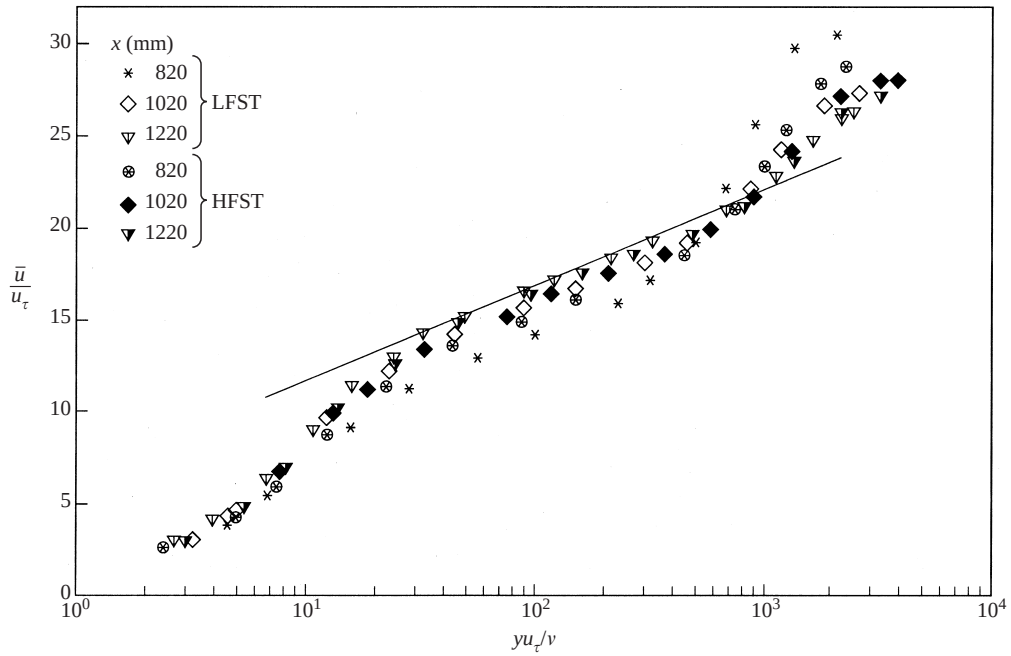

FIGURE 12. Mean velocity profiles in inner-law scaling (NHW-data) downstream of reattachment for LFST and HFST (for characteristic parameters see table 2).

values larger than in a canonical boundary layer if the FST-level is high enough (figure 13*b*). The $\overline{w'^2}$- and $\overline{v'^2}$-profiles are also higher for HFST but are not shown for lack of space. So the starting conditions of the three boundary layers are different for the development of the turbulence structure with and without free-stream turbulence. The boundary layer at $x = -5$ mm is in the initial region of the pressure rise without having gone through a fully developed ZPG region upstream. A comparison of LFST with the DNS data of Spalart 1988 – the Reynolds numbers are 1410 and 1354, respectively – shows good agreement for the measurements of u^+, $\overline{u'^2}/u_\tau^2$ and $\overline{u'v'}/u_\tau^2$ but the values for the measured $\overline{v'^2}/u_\tau^2$ and $\overline{w'^2}/u_\tau^2$ are 30% higher in the inner layer.

This comparison between the Reynolds stress profiles in the upstream and downstream region shows that FST strongly influences the state of the turbulence structure of the outer layer (this will be discussed below).

4. Flow properties in the reverse-flow region with and without FST manipulation

Since the pressure-driven reverse-flow region (case LFST) belongs to the category of weak reverse flows, the peak skin-friction coefficient $c_{f_{ref}}$ in the bubble is small, not exceeding 5% of the starting value at $x = -5$ mm (figure 6). The peak reverse-flow velocity is 10% of u_δ and although the bubble has a length of 217 mm it is shallow with a maximum height $y_{\psi=0} = 19.5$ mm. The extent of the bubble normal to the wall may also be seen from the profiles of the mean velocity (figure 9) and of the reverse-flow factor χ (figure 8), and in the streamwise direction by the distributions of c_f and χ_w (figure 6). We can assume here that the effects of streamwise curvature on the separated shear layer are much smaller than in the flow configurations of the

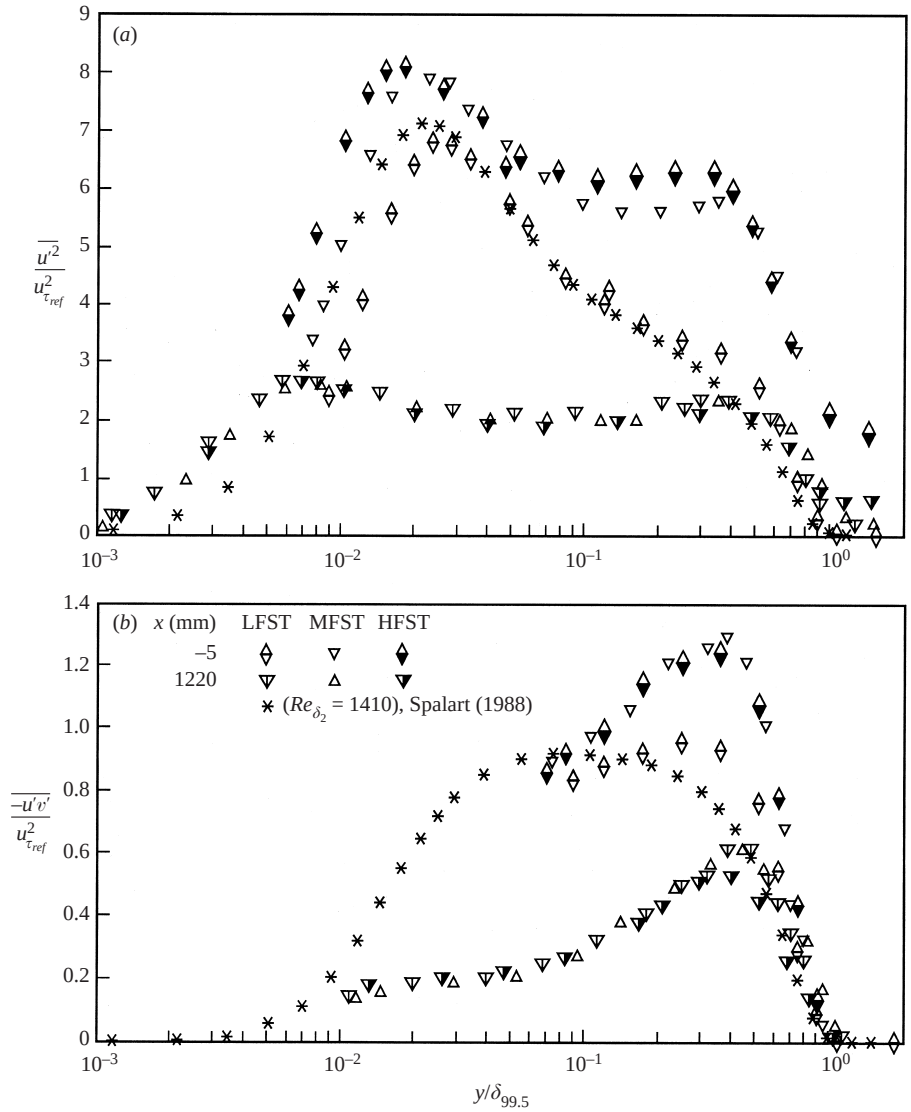

FIGURE 13. Comparison of the effect of the FST on Reynolds stress profiles in an undisturbed and a highly disturbed boundary layer.

blunt flat plate or the normal flat plate followed by a splitter plate. Curvature effects on the separated shear layer only play a role for the turbulence structure for LFST and MFST but not for HFST where there is no mean separation. In the first two cases the ratio $2\eta_m/\Delta x_R$ is 0.100 and 0.037 respectively, where η_m is the maximum height of the bubble at $y_{max}(\overline{u} = 0)$ and Δx_R the distance between separation and reattachment).

The discussion of the turbulence structure begins with wall data, i.e. with higher moments of the fluctuating skin friction c'_f, S_w, and F_w (figure 14). They are defined as

$$c'_{f_{ref}} = \frac{2\tau'_{w_{rms}}}{\overline{\rho} U^2_{ref}}, \tag{4.1}$$

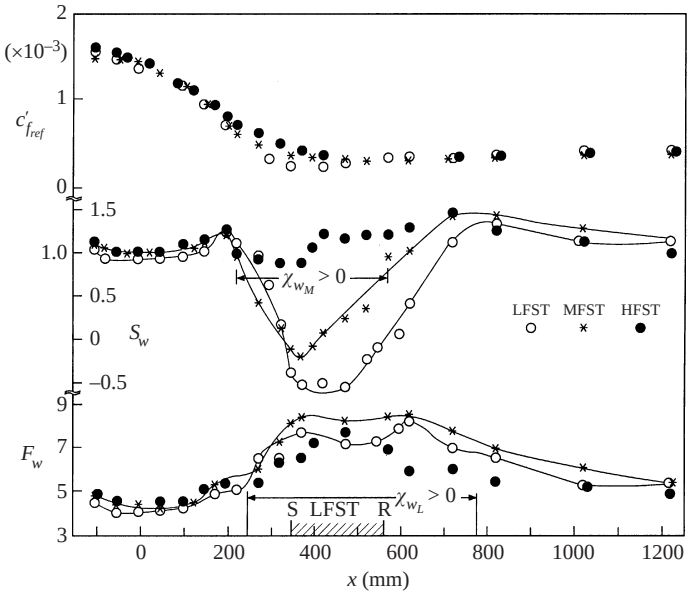

FIGURE 14. Moments of the fluctuating skin friction c'_f, the skewness S_w and the flatness F_w for LFST, MFST and HFST (lines are for visual aid only).

$$S_w = \frac{\overline{\tau_w'^3}}{(\overline{\tau_w'^2})^{3/2}}, \tag{4.2}$$

$$F_w = \frac{\overline{\tau_w'^4}}{(\overline{\tau_w'^2})^2}. \tag{4.3}$$

c'_{fref} shows the familiar decrease in an APG (see e.g. AF; DF) and remains almost constant downstream of separation. It is practically unaffected by FST and by mean (LFST and MFST) or instantaneous reverse flow (HFST).

The distribution of the skewness S_w for LFST displays much the same behaviour as in AF, beginning at $S_w \approx 1$, as in the canonical boundary layer, and decreasing where the reverse-flow factor χ_w begins to increase from zero. S_w, being an odd moment, changes sign at separation and again at reattachment, with an almost constant value of -0.5 over the centre of the bubble. For MFST the S_w distribution is similar to that of LFST, again showing a marked drop, but due to the shorter reverse-flow region it does not establish a range with a constant low value. Separation ($S_w = 0$) for LFST and MFST is approximately at the same position. For HFST the peak reverse-flow factor $\chi_w = 12\%$ and the decrease of S_w is less than 15% of the initial value, remaining positive over the whole distance of the instantaneous reverse-flow region. Downstream from reattachment S_w shows a slight overshoot before it falls to $S_w \approx 1$ in all three cases.

The wall flatness factor F_w is about 4 in a canonical boundary layer (e.g. Fernholz & Finley 1996). In an APG region F_w increases, rising even more with the onset of reverse flow. It forms a plateau at $F_w = 8$ for LFST and MFST. For HFST F_w rises substantially to about 7 without establishing a plateau, extending over the distance where χ_w is larger than zero. High values of the flatness imply the intermittent mixing of turbulent and quiescent fluid. This could be caused in the reverse-flow region by lumps of fluid from the separated shear layer hitting the near-wall region (Wagner

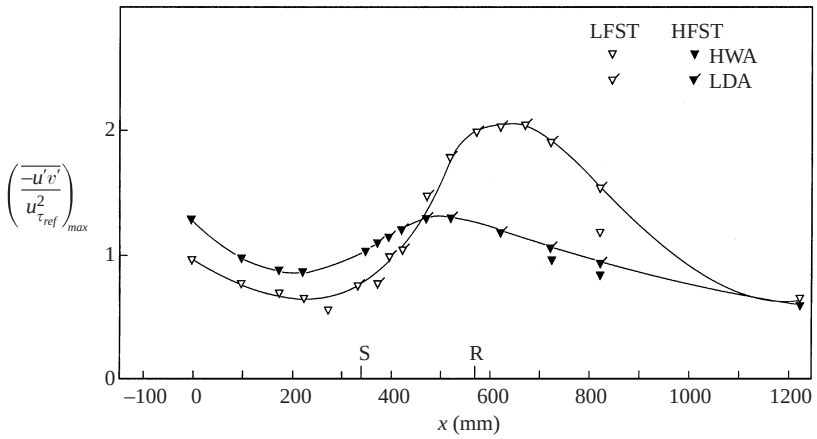

FIGURE 15. Streamwise development of the maximum values of the Reynolds shear stress for LFST and HFST (lines are for visual aid only).

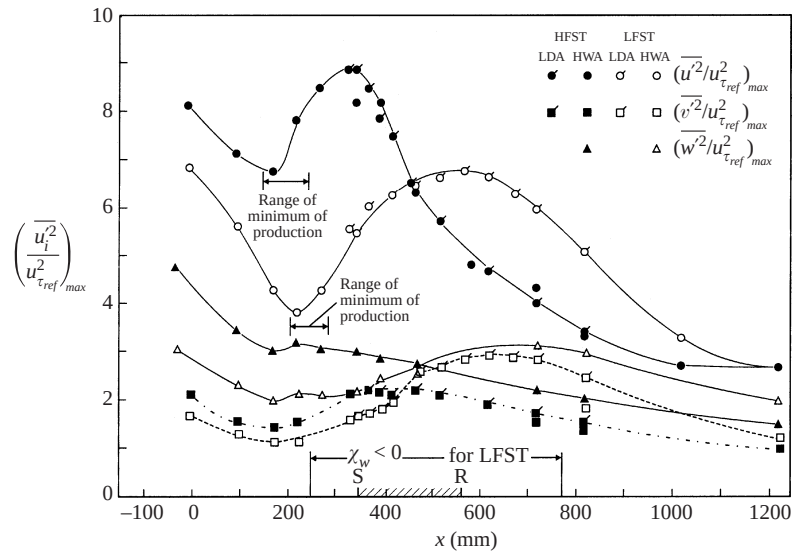

FIGURE 16. Streamwise development of the maximum values of the Reynolds normal stress for LFST and HFST (lines are for visual aid only).

1995; Fernholz 1994). For HFST the increased vertical velocity fluctuations transport higher energy fluid towards the wall, achieving a slightly smaller value of F_w. This type of energy transport (see figure 21 below) is effective also downstream of reattachment since F_w does not fall to a value typical of the canonical boundary layer.

For the boundary layer with LFST the present measurements may be compared with those of AF and show good agreement. Before we present Reynolds stress profiles in the reverse-flow region, the variation of the maximum values of the Reynolds shear (figure 15) and Reynolds normal stresses (figure 16) are shown in the streamwise direction for LFST and HFST. The maximum values are non-dimensionalized by the skin-friction velocity $u_{\tau_{ref}}$ at the upstream station ($x = -5$ mm).

All streamwise distributions of the Reynolds stress maxima have in common that they decrease in the APG region from their typical value in the canonical boundary

layer to a minimum at approximately $x \approx 170\,\text{mm}$, a position where the mean velocity profiles begin to deviate from the logarithmic law (figure 11) and where the production minimum is located. For LFST the Reynolds stresses reach a maximum at or just upstream of reattachment. $(\overline{u'v'})_{max}$ and $(\overline{u'^2})_{max}$ falling then rather steeply to values below their upstream starting values. This sudden fall is explained by Castro & Epik (1998) as being due to the rapid disintegration of the paired eddies in the separated shear layer which stretch and distort beyond reattachment and the subsequent development of smaller-scale motions.

For HFST the peaks of $\overline{u'^2}$ and $\overline{u'v'}$ downstream of the relative minimum lead those of LFST but the maximum value is higher for $\overline{u'^2}$ and lower for $\overline{u'v'}$ when FST is added. This behaviour will be discussed together with the production and turbulent diffusion terms of the turbulent kinetic energy. The fall in $(\overline{u'^2}/u^2_{\tau_{ref}})_{max}$ downstream of the peak is steeper than for LFST which would point to an even faster development of small-scale motions if the above argument were correct. The maximum values of the respective Reynolds stresses for LFST and HFST converge to almost the same value at the last measuring station ($\overline{w'^2}$ behaves slightly differently). The distribution of the maximum of the Reynolds stresses in the redevelopment region backs the conclusion drawn by Castro & Epik (1998) that the features of the developing boundary layer are qualitatively independent of the precise nature of the separation and reattachment process upstream.

The differences in the turbulence structure will become more evident if one compares the Reynolds stress profiles of LFST (with mean reverse flow and a mildly curved reattaching shear layer) with those of HFST, where the flow is modified by free-stream turbulence but has no mean reverse-flow region. These profiles will be discussed in connection with the production terms $\overline{u'v'}\,\partial\overline{u}/\partial y$ and $\overline{v'^2}\,\partial\overline{u}/\partial y$ for $\overline{u'^2}$ and $\overline{u'v'}$, respectively, and with the turbulent transport term $\overline{u'^2v'}$.

Selected profiles of the four Reynolds stresses $\overline{u'^2_{ij}}/u^2_{\tau_{ref}}$ are plotted in figures 17 and 18 against $y/\delta_{99.5\%}$ to show their development in the streamwise direction and the location and growth of the stress peaks. For scaling we have used $u_{\tau_{ref}}$ and y/δ in order to avoid u_τ and ν/u_τ in regions close to separation. The logarithmic scale of the abscissa, however, allows a qualitative comparison with the graphs plotted against y^+. All profiles where reverse flow occurred were measured by LDA (note there are no w'-data). The series of profiles in each figure begins in the initial region of the pressure rise and ends at the last downstream station. For LFST, until the end of separation, the behaviour of the profiles is characteristic of that seen in other APG flows (e.g. AF; DF).

The location of $(\overline{u'^2}/u^2_{\tau_{ref}})_{max}$ moves from the wall region ($y/\delta \approx 0.002$ or $y^+ = 14$ at $x = -5\,\text{mm}$) to roughly the middle of the boundary layer for LFST and HFST (figure 17*a*, *b*). In the profiles further downstream, the magnitude of the peak decreases near the wall and increases in the outer layer until downstream of reattachment to approximately the initial value at $x = -5\,\text{mm}$ (cf. figure 13*a*). The outer-layer peaks of the Reynolds stresses near reattachment (for LFST) are reflected by peaks of the respective production terms $\overline{u'v'}\,\partial\overline{u}/\partial y$ and $\overline{v'^2}\partial\overline{u}/\partial y$ slightly upstream ($x = 470\,\text{mm}$). The production terms are plotted non-dimensionalized in figures 19 and 20. The height of the peaks in the outer layer decreases downstream of reattachment, but the initial peak in the inner layer is not regained, thus showing a reason for the underdeveloped turbulence structure in the inner layer at the end of the test section. This is a feature of all Reynolds stress profiles with and without FST in APG flows with separation (see AF and Castro & Epik 1998, for example). As was mentioned above, FST affects

the profiles of the streamwise and spanwise Reynolds normal stresses in the outer region (figure 17*b*, *d*) in that the profiles are fuller in the outer region and the peaks higher until they reach the end of the streamwise pressure rise. Then, however, the peak of the profiles decreases faster (see also Castro & Epik 1998) and the profile size shrinks more than that of their counterparts of LFST (figure 17*a*, *c*) and the difference between the profiles at $x = 95$ mm and $x = 1220$ mm is distinctly larger.

The $\overline{w'^2}$-profiles under FST are fuller and have higher peaks in the outer region of the boundary layer while the pressure is rising. They then decrease rapidly forming a plateau over the centre of the boundary layer which lies below the profiles for LFST. In the redeveloping shear layer the $\overline{w'^2}$-profiles do not recover the equivalent profiles of the canonical boundary layer (see Fernholz & Finley 1996, their figure 51). The increase of $\overline{w'^2}$ beyond $y/\delta = 1$ in the downstream region is probably a sign of the boundary layers on the two concentric walls approaching each other.

The influence of the FST on $\overline{v'^2}$ and $\overline{u'v'}$ is clearly smaller and the peaks of the profiles for LFST (figures 18*a* and 18*c*) in the reattachment region ($x = 620$ mm) exceed those at the same position for the HFST flow (figures 18*b* and 18*d*).

For LFST the $\overline{v'^2}$ and $\overline{u'v'}$ profiles regain the values of the initial peak in the outer layer (figures 18*a* and 18*c*) in the redevelopment region but this is not the case for the flow with FST where the profiles of all Reynolds stresses at the last measuring station remain far below their initial values upstream (figures 17*b*, *d* and 18*b*, *d*). In the inner layer there is little difference between the profiles ($\overline{v'^2}$ and $\overline{u'v'}$) with and without FST which is reflected by the small recovery of the production in figure 20(*a*, *b*).

The profiles of the Reynolds stresses $\overline{v'^2}$ and $\overline{u'v'}$ (figure 18) have in common that their peaks are located approximately in the middle of the boundary layer and that the profiles grow from the beginning to the end of the streamwise pressure rise. This is again in agreement with the development of the production term profiles for the Reynolds shear stress $\overline{v'^2}(\partial\overline{u}/\partial y)\delta_1/{u_\delta}^3$ presented in figure 20(*a*, *b*).

For HFST the peaks of the production profiles in the outer layer (figures 19*b* and 20*b*) are smaller by a factor of 3 compared with those of LFST and so the increase of $\overline{u'^2}$ (figure 17*b*) must be achieved by strong additional turbulent transport via diffusion (figure 21).

The triple correlation $\overline{u'^2v'}$ appears in the turbulent diffusion term $\partial\overline{u'^2v'}/\partial y$ and we discuss it here by direct reference to the triple product rather than to its gradient, following Murlis, Tsai & Bradshaw (1982). $\overline{u'^2v'}$ accounts for the transport of $\overline{u'^2}$ by the wall-normal velocity fluctuations v' and reflects, in the near-wall region, wall-normal transport of inner-layer fluid. Near the wall it is related to the spanwise vorticity ω_z' by

$$-\frac{\partial\overline{u'^2v'}}{\partial y} = -2\overline{u'v'\frac{\partial u'}{\partial y}} - \overline{u'^2\frac{\partial v'}{\partial y}} \approx +2\overline{u'v'\omega_z'} - \overline{u'^2\frac{\partial v'}{\partial y}}. \tag{4.4}$$

Sendstadt & Moin (1992) point out that streaks are associated with large streamwise fluctuations, u', normal vorticity ω_y and spanwise vorticity fluctuations ω_z'. Both positive and negative values of $\overline{u'^2v'}$ occur and the minimum value of -1 is at about $y/\delta = 0.2$ for LFST or at $y^+ \approx 140$ for HFST. The positive peaks occur in the outer layer at about $y/\delta = 0.7$ with the profiles of LFST narrower but with much higher peaks than those of HFST, suggesting a transport peak in the reattachment region and transport over a broader part of the outer layer in the same region for HFST. In both cases the peaks in the outer layer flatten out to a plateau further downstream.

Figure 22 presents the positive and negative peaks of the turbulent transport profiles showing higher values for HFST in the region of the streamwise pressure rise and

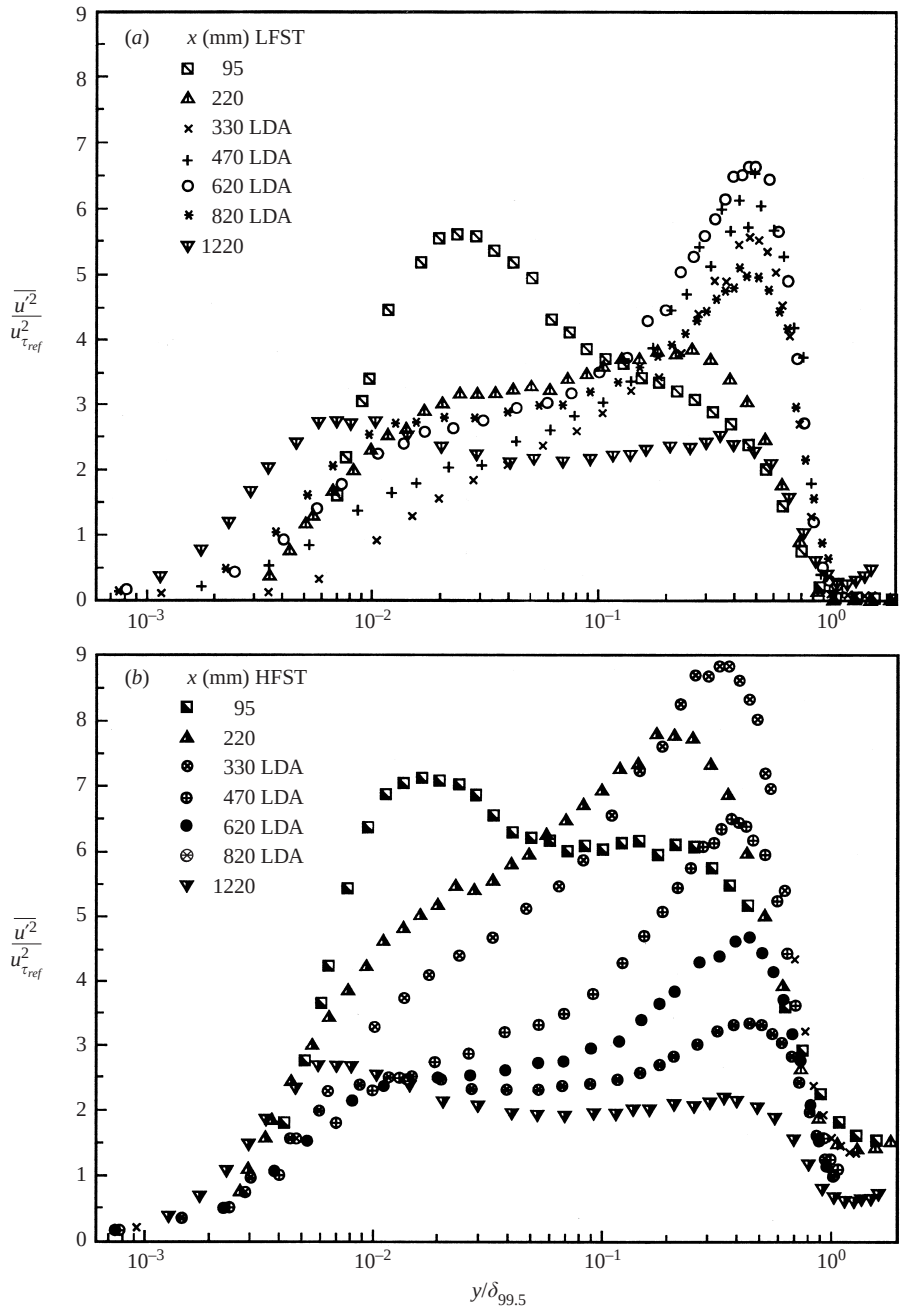

FIGURE 17(*a*, *b*). For caption see facing page.

higher values for LFST in the reattachment and redevelopment region. In this latter region large discrepancies of up to 100% occur between hot-wire and LDA-data which are due to the instantaneous reverse flow on the one hand and the very high turbulence levels on the other.

The influence of FST on the structure parameter $a_1 = \overline{u'v'}/(\overline{u'^2}+\overline{v'^2}+\overline{w'^2})$ at the first ($x = -5$ mm) and the last ($x = 1220$ mm) measuring station is presented in figure 23.

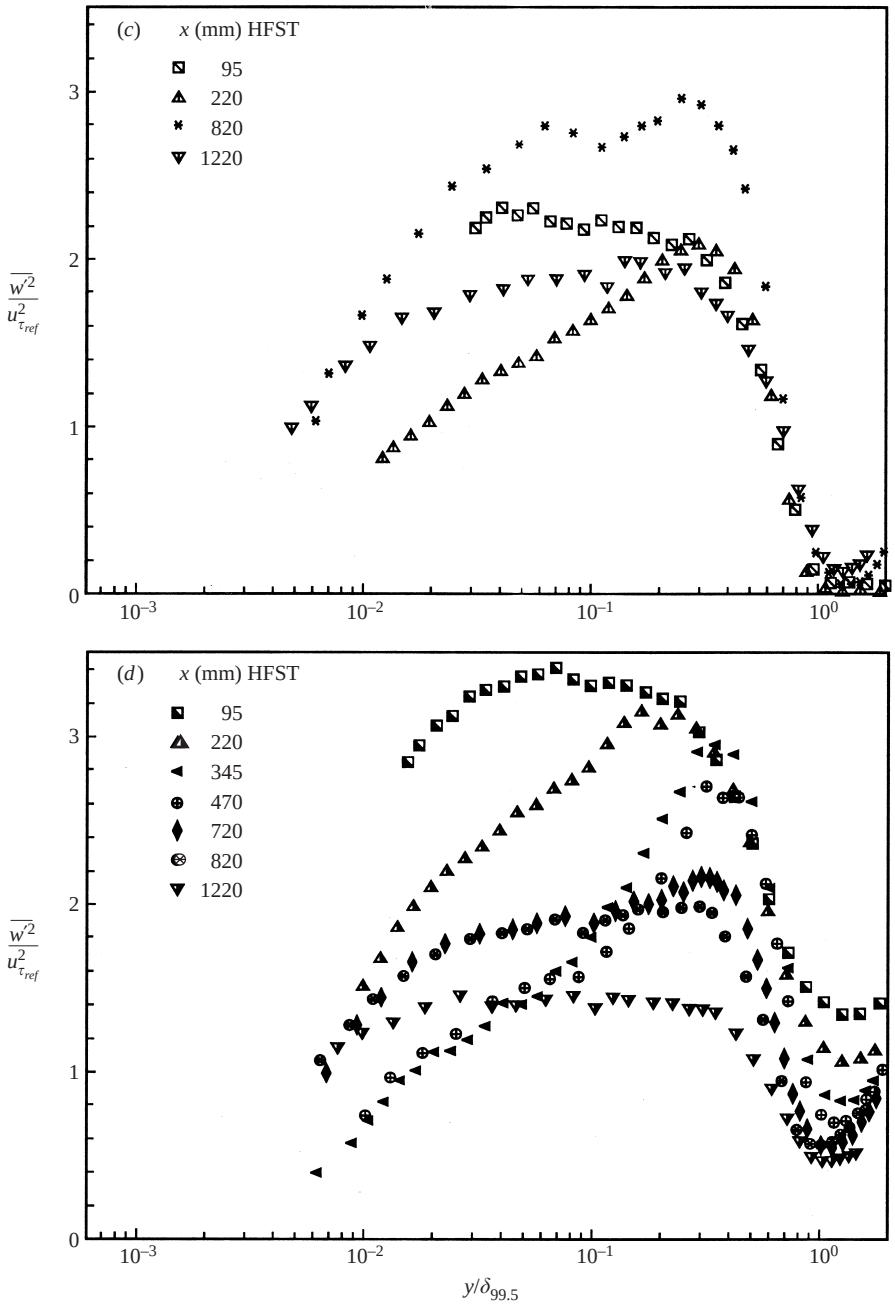

FIGURE 17. Streamwise and spanwise components of the Reynolds normal stress: (a, b) $\overline{u'^2}/u^2_{\tau_{ref}}$ and (c, d) $\overline{w'^2}/u^2_{\tau_{ref}}$ for LFST and HFST.

A comparison with data of a canonical boundary layer (Erm 1988, $Re_{\delta_2} = 1567$) shows that the first a_1-profile is already affected by the APG. For the ZPG boundary layer the variation of a_1 lies between 0.15 and 0.16 in the range $0.15 \leqslant y/\delta \leqslant 0.80$. At the first profile ($x = -5$ mm) this plateau is much narrower due to the beginning pressure gradient. The level of a_1 decreases with increasing FST due to the stronger increase of the Reynolds normal stresses compared with that of the shear stress.

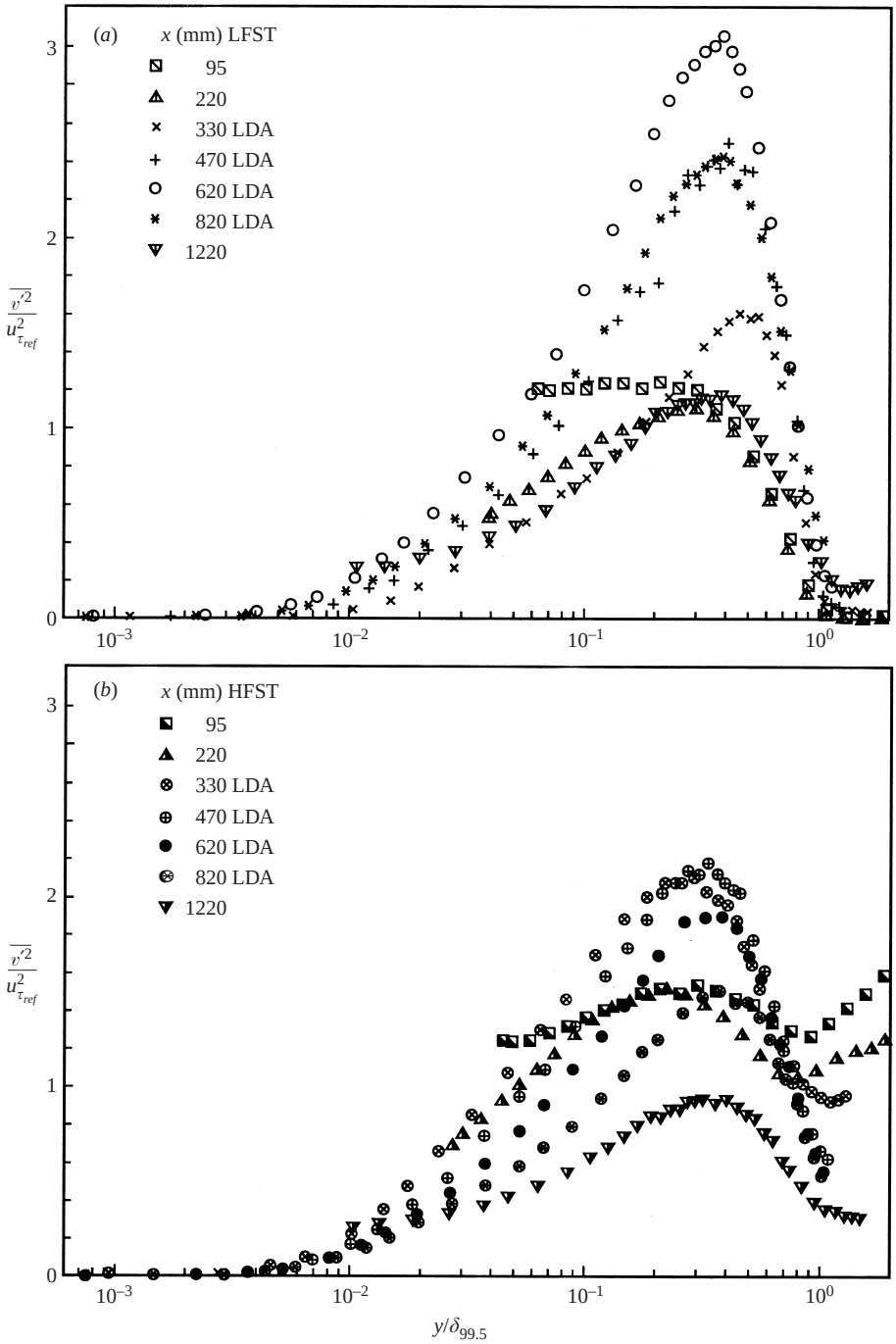

FIGURE 18(*a*, *b*). For caption see facing page.

Figure 24 presents a_1-profiles at eight stations for LFST and HFST. Progressing in the downstream direction, a_1 drops across the boundary layer reflecting the Reynolds stress development in an APG boundary layer (see for example Dengel 1992) with a decrease in overall level by about 50%. In the ZPG region the peak value of a_1 rises almost to its initial value in the outer layer at $x = 1220$ mm but the profile values

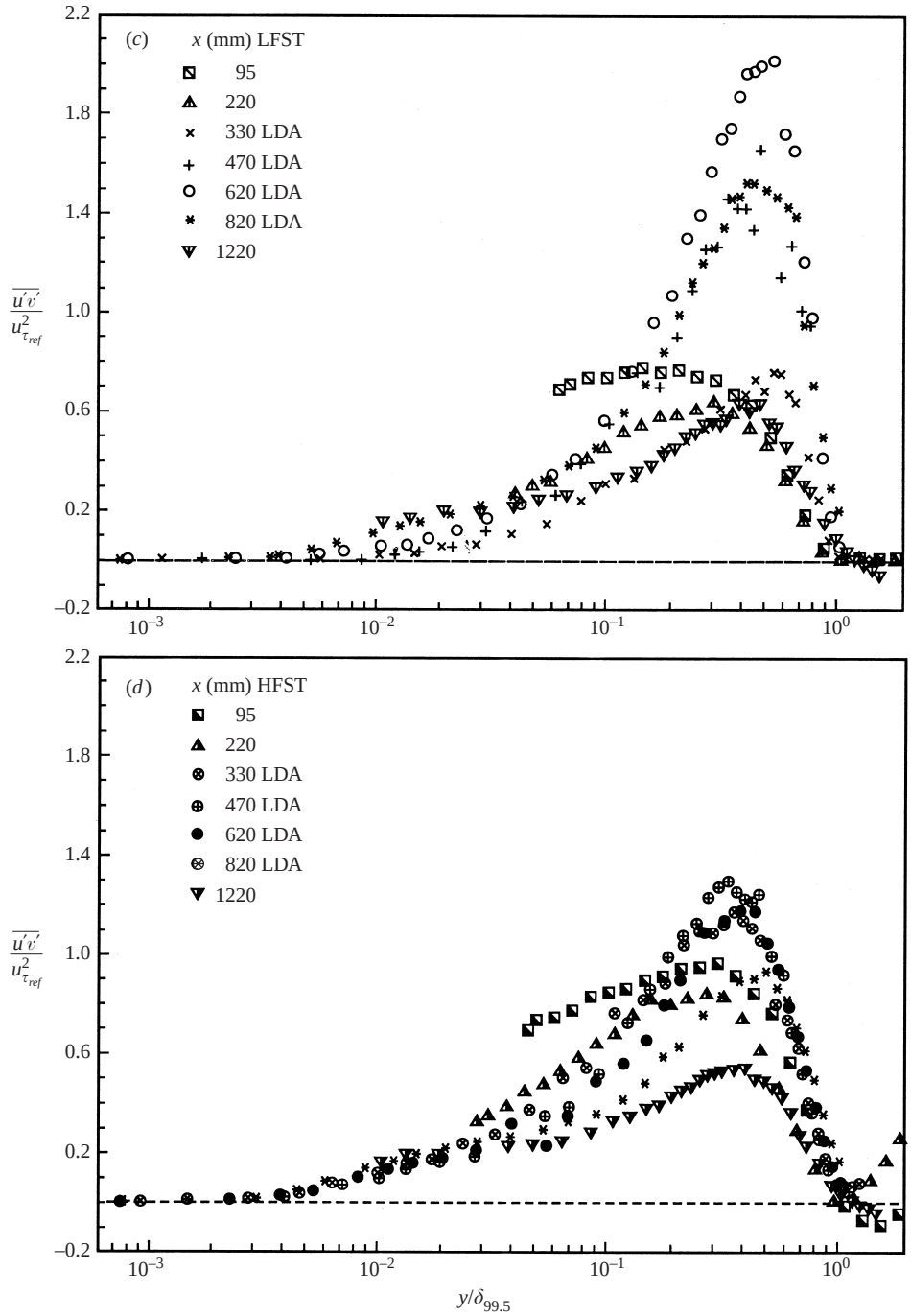

FIGURE 18. Wall-normal component of the Reynolds normal stress and Reynolds shear stress: (a, b) $\overline{v'^2}/u^2_{\tau_{ref}}$ and (c, d) $\overline{u'v'}/u^2_{\tau_{ref}}$ for LFST and HFST.

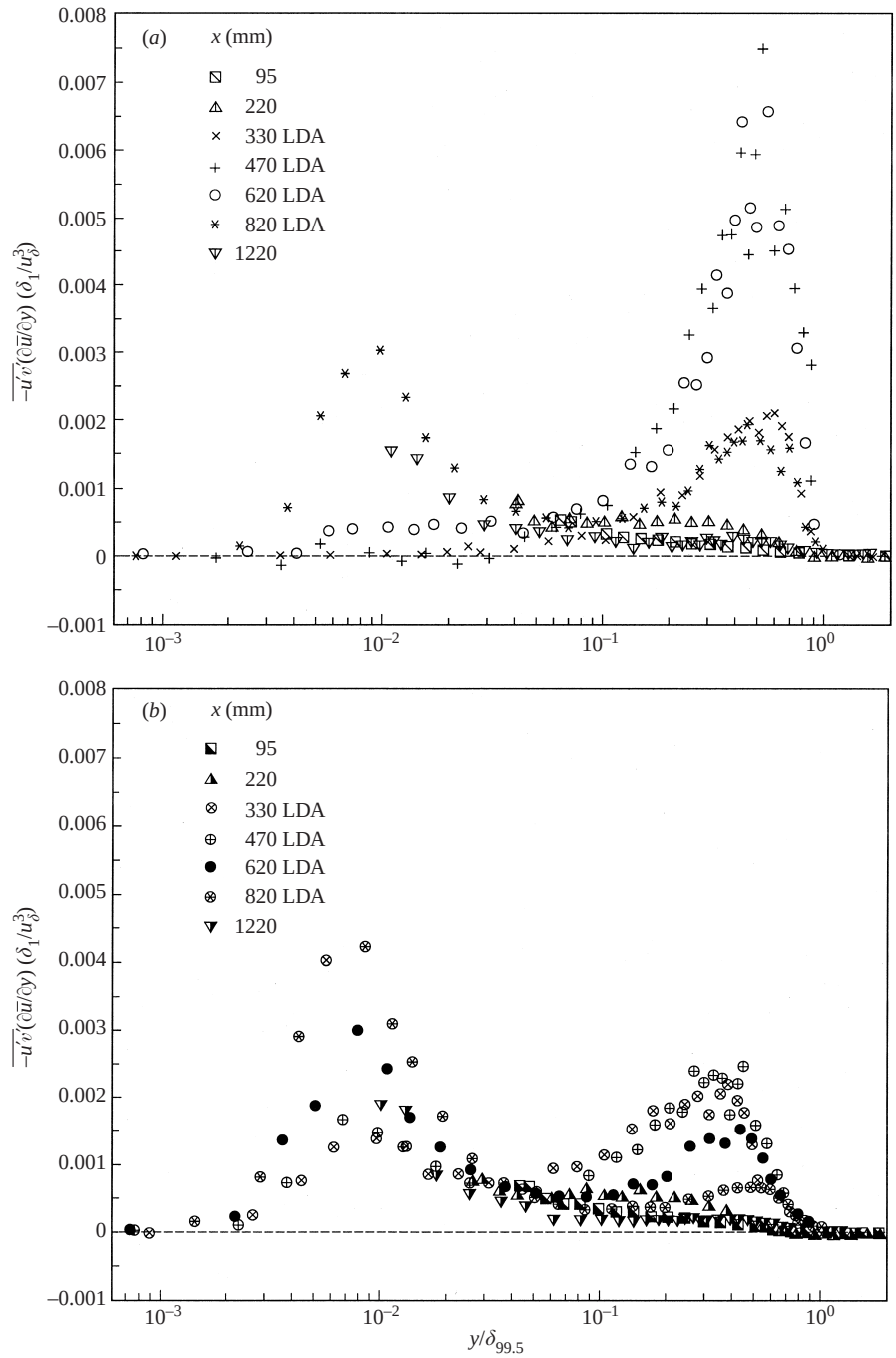

FIGURE 19. Streamwise development of the profiles of the production term $\overline{u'v'}(\partial\overline{u}/\partial y)\delta_1/{u_\delta}^3$ for (*a*) LFST and (*b*) HFST.

remain small in the inner layer throughout (see also AF; Kalter 2001). Thus the profiles of the structure parameter confirm the unusual behaviour of the Reynolds stresses in the inner region of the HFST boundary layer as compared with that in a canonical boundary layer. Qualitatively, although not in detail, our results agree with those of Castro & Epik (1998).

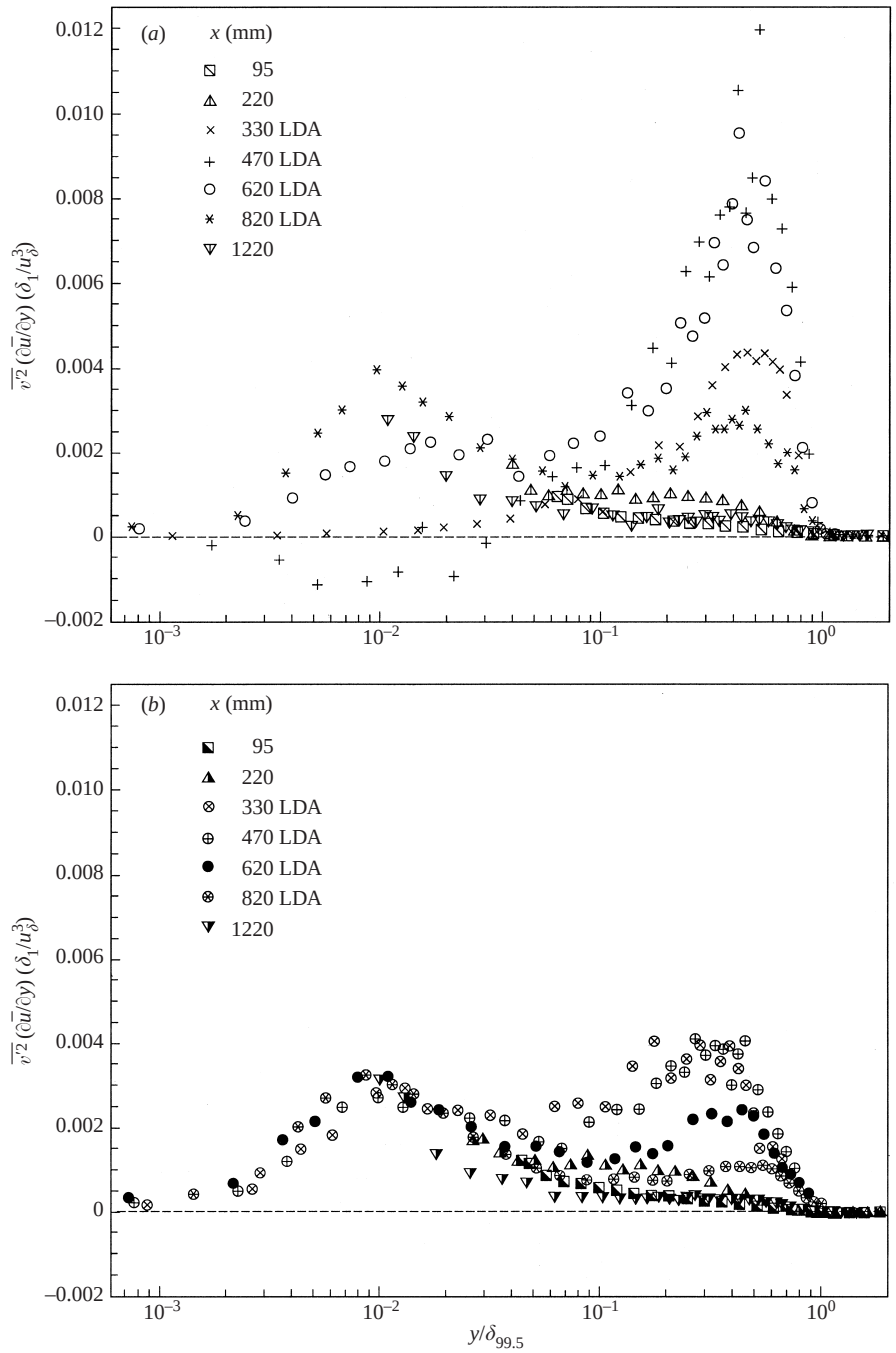

FIGURE 20. Streamwise development of the profiles of the production term $\overline{v'^2}(\partial\overline{u}/\partial y)\delta_1/u_\delta{}^3$ for LFST and HFST.

Returning to figure 23 and the last measuring station ($x = 1220$ mm) one notes that the a_1-profiles lie very close to each other despite the different levels of the FST at the upstream end and despite the different initial conditions for the developing boundary layer.

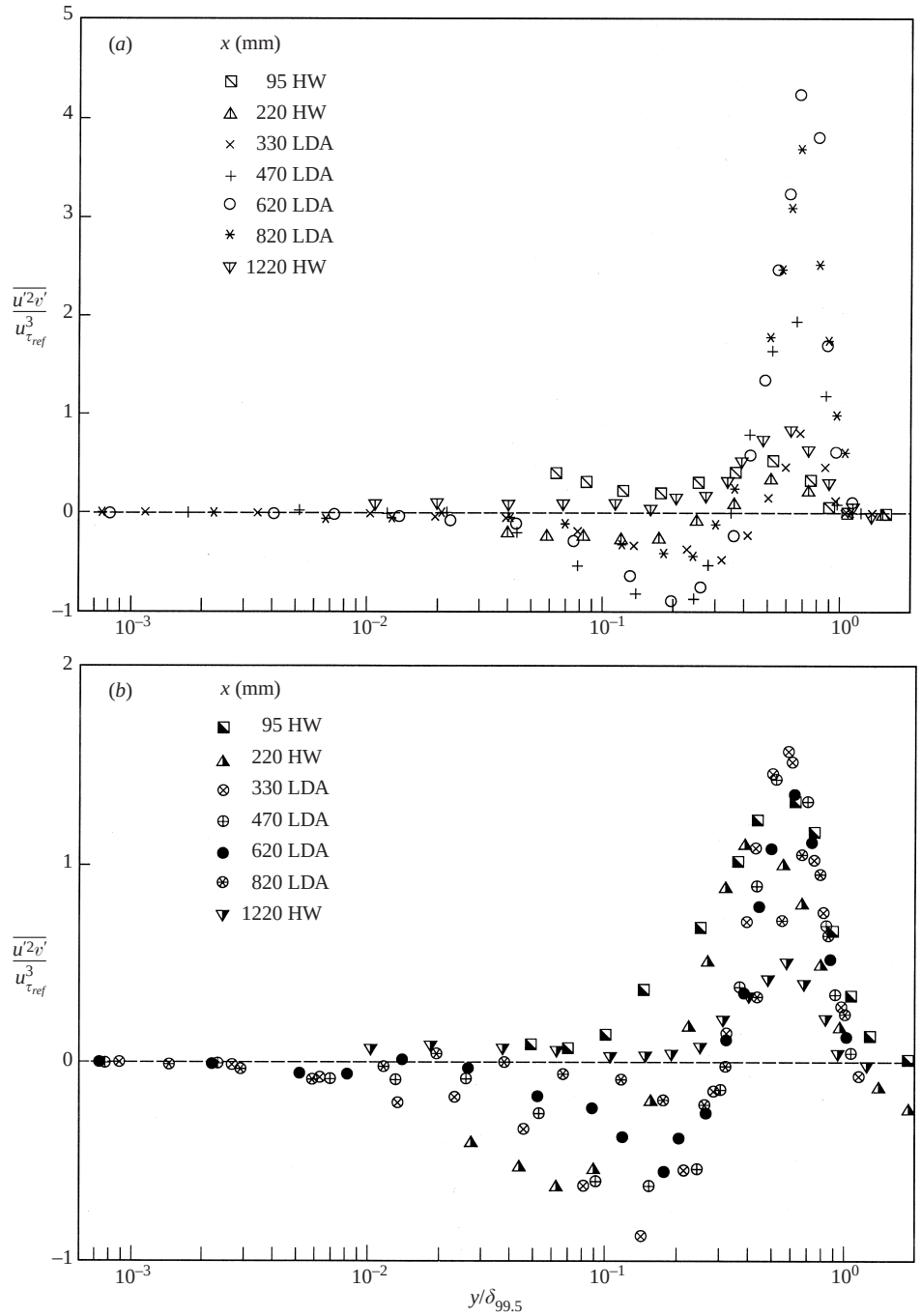

FIGURE 21. Distribution of the profiles of the turbulent transport term $\overline{u'^2v'}/u^3_{\tau_{ref}}$ at various x-stations. (*a*) LFST and (*b*) HFST.

The profiles of the skewness S_u and flatness F_u distributions across the boundary layer (figure 25*a*, *b*) show an effect – although not large – of the pressure gradient when compared with the respective profiles in a canonical boundary layer (Fernholz & Finley 1996, their figure 66). For LFST pressure gradient and reverse-flow lead to an

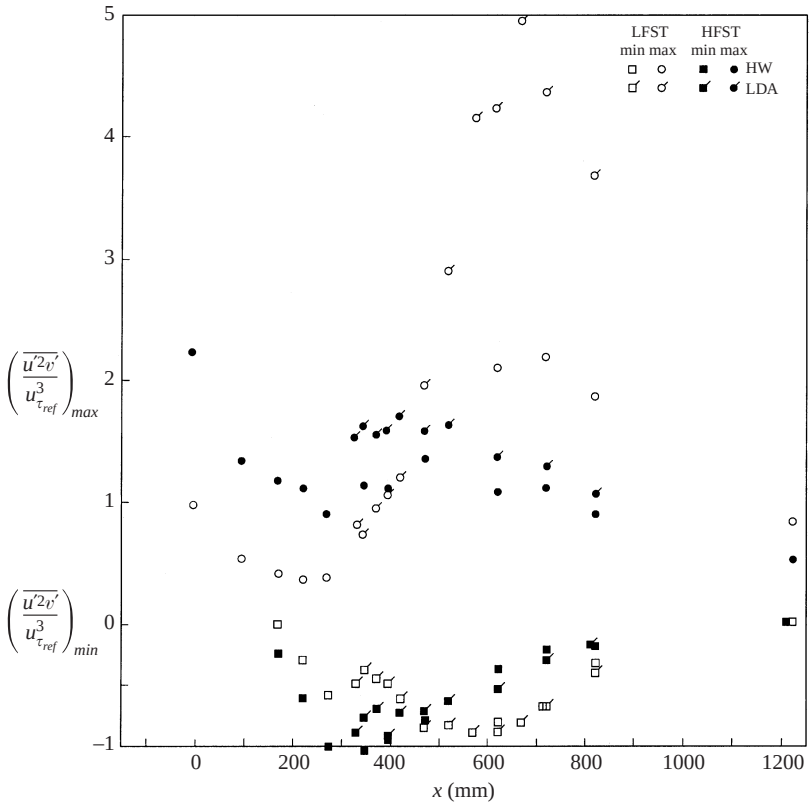

FIGURE 22. Streamwise distribution of the maxima and minima of $\overline{u'^2v'}/u^3_{\tau_{ref}}$ for LFST and HFST.

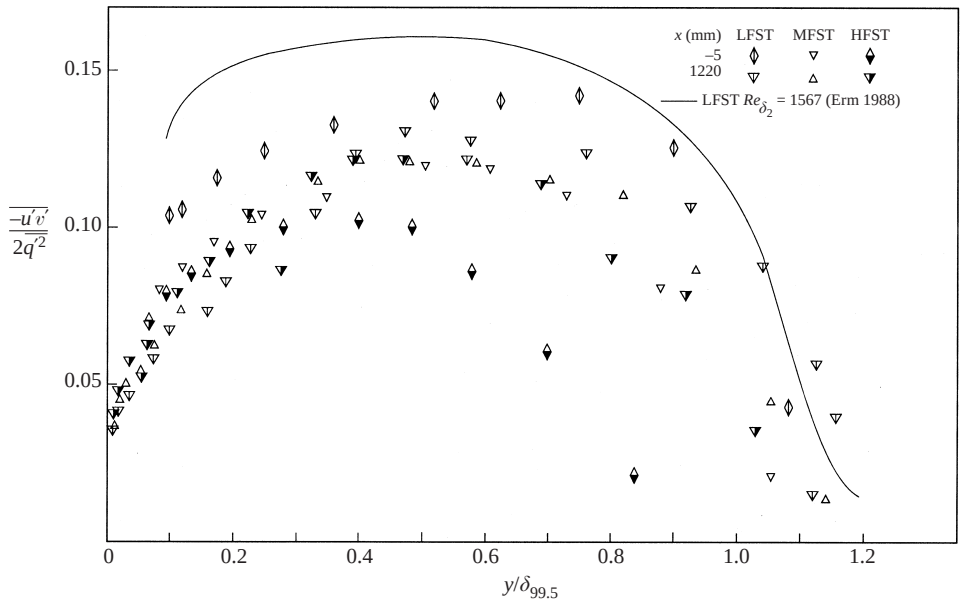

FIGURE 23. Comparison of the effect of FST on the structure parameter a_1 in an undisturbed and a highly disturbed boundary layer.

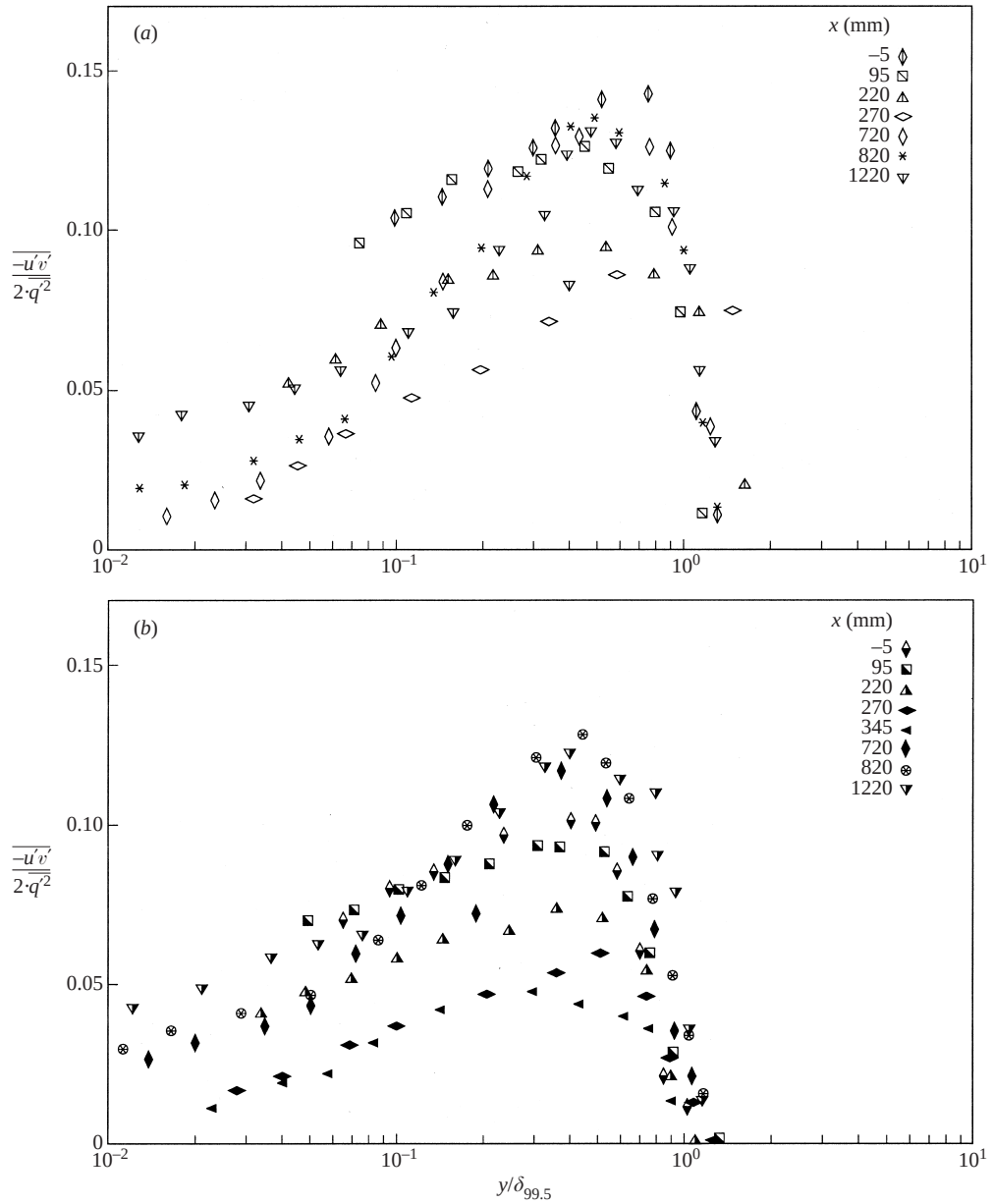

FIGURE 24. Profiles of the structure parameter $\overline{u'v'}/(\overline{u'^2}+\overline{v'^2}+\overline{w'^2})$ upstream and downstream of the reverse-flow region for (*a*) LFST and (*b*) HFST.

increase of both S_u and F_u in the inner region of the boundary layer ($0.01 \leqslant y/\delta \leqslant 0.3$) with the maximum values at about reattachment. These results are in agreement with the data of AF.

For HFST the effect of the pressure gradient is reduced by the free-stream turbulence in that the profiles of figure 25*b* lie in a narrower band. At the outer edge of the boundary layer F_u becomes much smaller for HFST reflecting a less convoluted outer edge. In the near-wall region the peaks of S_u and F_u have almost the same values and the same location above the wall in both cases, showing little effect of either pressure gradient or of free-stream turbulence.

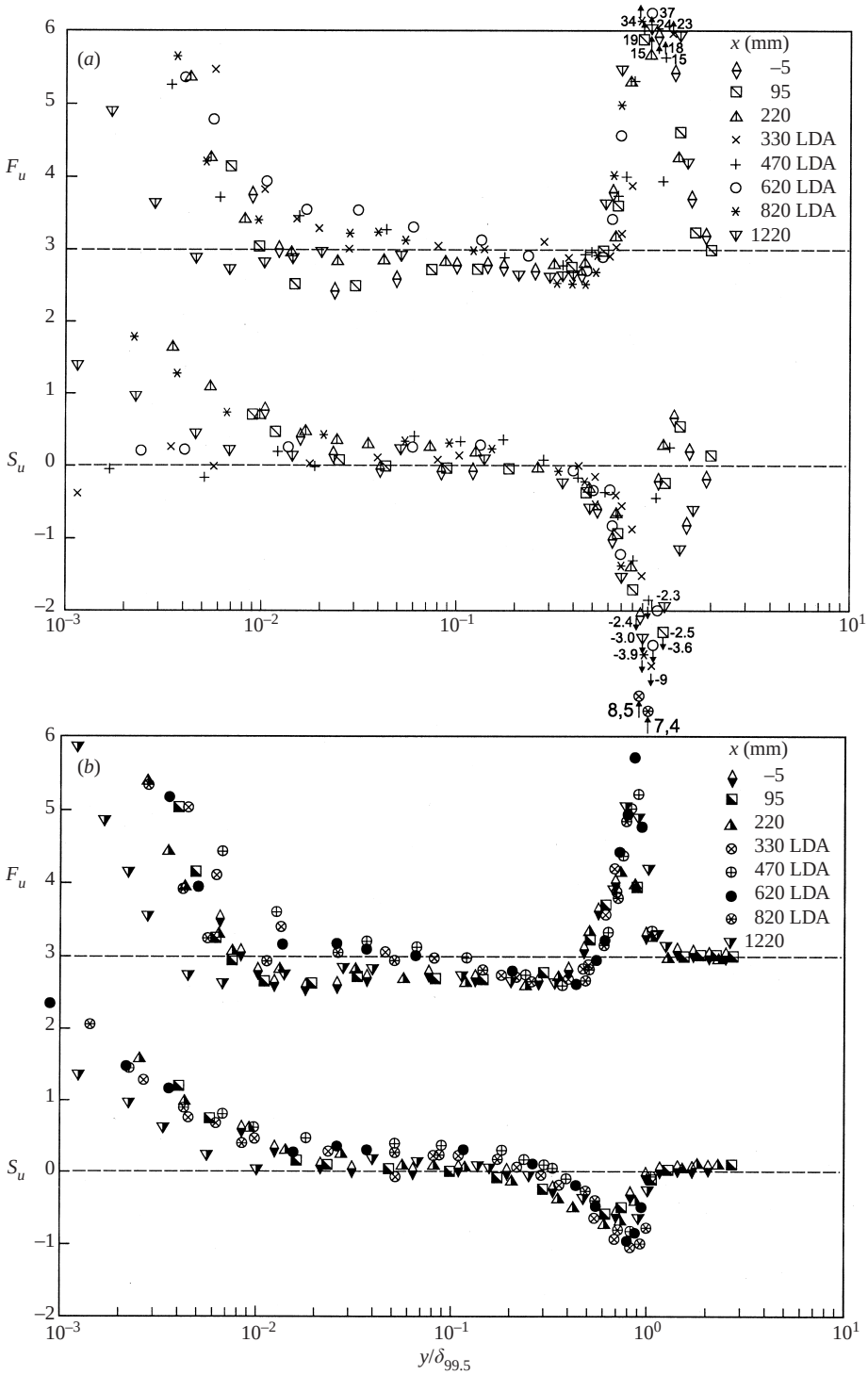

FIGURE 25. Profiles of the skewness S_u and flatness F_u distributions across the boundary layer for (*a*) LFST and (*b*) HFST.

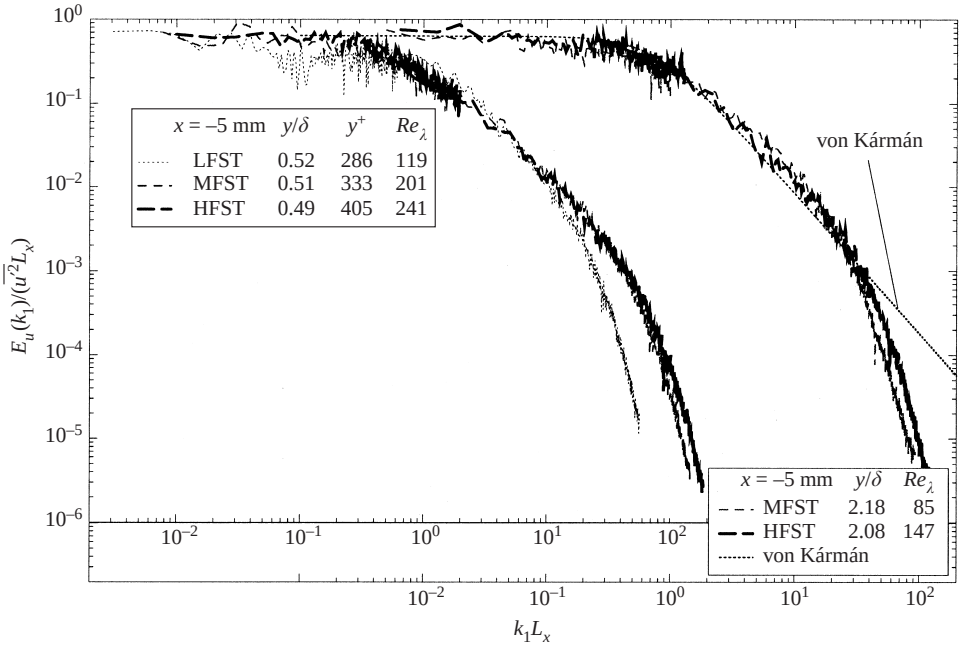

FIGURE 26. Longitudinal wavenumber spectra $E_u(k_1)$ scaled by the variance $\overline{u'^2}$ and the integral length scale L_x.

At the end of this section we present the influence of FST on the spectra of the upstream APG and the highly disturbed downstream boundary layer at four x-positions for LFST and HFST (for further details the reader is referred to Kalter 2001). The one-dimensional wavenumber spectra $E_u(k_1)$ were determined from the power spectral density $E_u(f)$ using Taylor's hypothesis at locations where $\overline{u'^2}/\overline{u}$ was below 25%:

$$\int_0^\infty E_u(k_1)\mathrm{d}k_1 = \overline{u'^2}. \tag{4.5}$$

$E_u(f)$ was calculated from the linearized hot-wire signals using fast-Fourier transform routines given by Press *et al.* (1988). The longitudinal wavenumber spectra $E_u(k_1)$ are usually scaled for the spectra in the free stream by the variance $\overline{u'^2}$ and the integral length scale L_x. They are shown at the upstream station ($x = -5$ mm) in figure 26 for MFST and HFST and collapse onto each other for $k_1L_x \leqslant 40$, well into the $k^{-5/3}$ range, agreeing also with the relationship of von Kármán which holds for grid-generated FST (see Bearman & Morel 1983):

$$\frac{E_u(k_1)}{\overline{u'^2}\,L_x} = \frac{2}{\pi}[1 + 1.8(k_1\,L_x)^2]^{-5/6}. \tag{4.6}$$

Inside the boundary layer ($y/\delta \approx 0.5$) this scaling is not so appropriate and the scaling needs to be changed to that of Kolmogorov (see figure 28). The development of the spectra in the streamwise direction (figure 27) for the HFST shows good agreement between the spectra to the end of the $k^{-5/3}$ range. In the k^{-4} range (as found by Kistler & Vrebalovich 1966) the spectra with the higher FST lie above the one at the start of the test section ($x = -5$ mm). The respective spectra for MFST (not shown here) are even closer in this range.

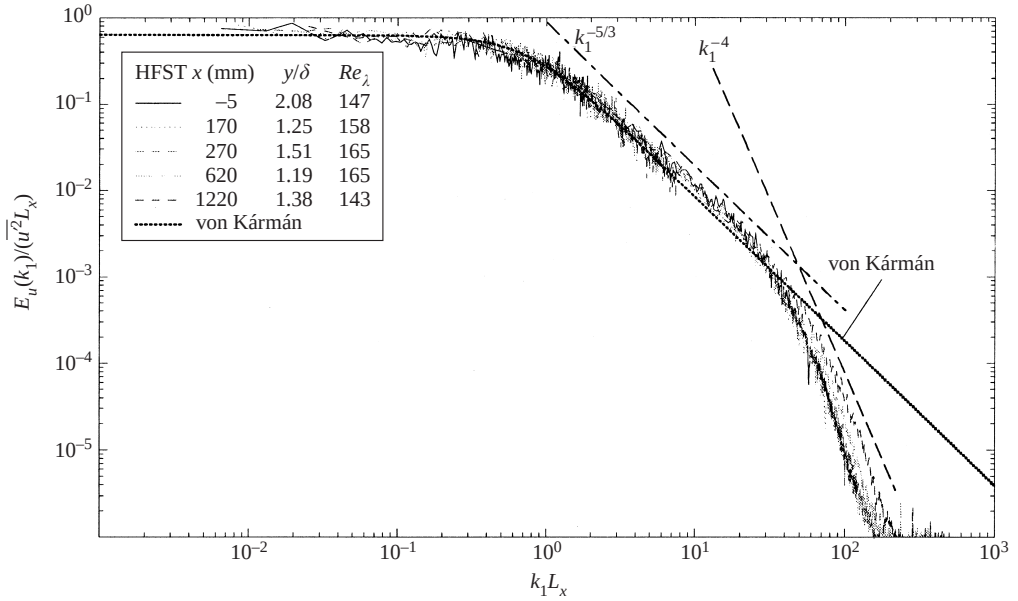

FIGURE 27. Development of the free-stream spectra in the streamwise direction for case HFST.

Figure 28 presents spectra at a fixed position normal to the wall ($y/\delta \approx 0.25$) at four x-stations for LFST (figure 28*a*) and HFST (figure 28*b*) in Kolmogorov scaling. Here the Kolmogorov length $\eta = (\nu^3/\epsilon)^{1/4}$ and the Kolmogorov velocity $v_k = (\nu\epsilon)^{1/4}$.

The dissipation ϵ was determined assuming isotropy (Hinze 1975) according to

$$\epsilon_{isotrop} = 15\nu\overline{\left(\frac{\partial u'}{\partial x}\right)^2} = 15\nu\frac{\overline{u'^2}}{\lambda_g^2} = 30\nu\frac{\overline{u'^2}}{\lambda_f^2} \tag{4.7}$$

with the Taylor microscale λ_f calculated from the integral of the one-dimensional dissipation spectrum (Hinze 1975, equation 1–102):

$$\frac{1}{\lambda_f^2} = \frac{2\pi^2}{\overline{u}^2\overline{u'^2}}\int_0^\infty f^2 E_u(f)\mathrm{d}f = \frac{1}{2\lambda_g^2}. \tag{4.8}$$

The legend of figure 28 also gives the respective location y^+ in the boundary layer and the usual turbulent Reynolds number $Re_\lambda = \lambda_g(\overline{u'^2})^{1/2}/\nu$ (it is common practice to follow G. I. Taylor in taking λ_g instead of λ_f, see Hinze 1975).

The spectra in the boundary layer with an APG and FST follow the pattern of those in the canonical boundary layer and collapse from the beginning of the inertial subrange of the equilibrium spectrum ($E \sim k^{-5/3}$) and at even higher wavenumbers. In the lower wavenumber range the influence of Re_λ can be detected, although the values of Re_λ differ within only a small range. An increasing FST level also leads to a higher level at smaller wavenumbers. In the latter case the k^{-1} range extends to lower wavenumbers.

5. Conclusions

An increase of the free-stream turbulence level from 0.2% to 5.6% was sufficient to eliminate a separation bubble of 217 mm length and 19.5 mm height in weak

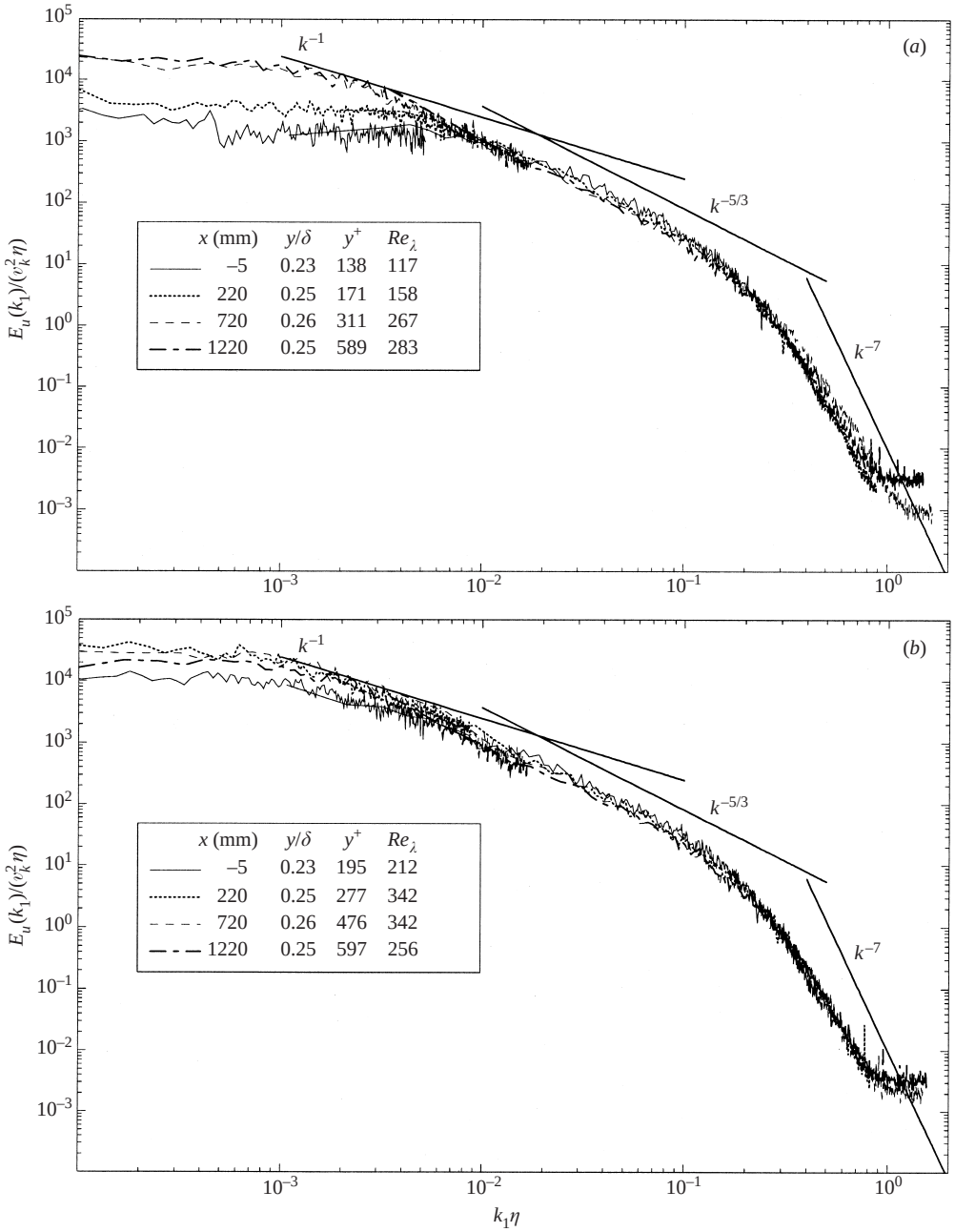

FIGURE 28. Development of the one-dimensional wavenumber spectra in the streamwise direction u' in Kolmogorov scaling at $y/\delta \approx 0.25$ at four x-positions (*a*) LFST (*b*) HFST.

reverse flow. The main objective has been to investigate the influence of FST on weak reverse-flow regions by using laser-Doppler anemometry and wall pulsed-wire probes. Measurements were taken of mean and fluctuating velocities and of skin friction.

A second goal was to document the development of the boundary layer downstream of the mean or instantaneous reverse-flow regions. This 'boundary layer' had been observed by AF to show a response to the strong upstream disturbance which is very

different from the usual relaxation process after a change in wall boundary conditions, in which an internal layer of regenerated stress would regrow into the outer layer (e.g. Smits & Wood 1985).

Three flow cases were investigated: case LFST with low FST, case MFST with medium FST and case HFST with high grid-generated FST with an initial intensity of 0.2%, 3.4% and 5.6%, respectively, and a turbulence length scale of the order of the boundary layer thickness (see § 3). Examination of the one-dimensional wavenumber spectra showed that the FST in the test section has the classic characteristics of grid-generated turbulence.

Although the turbulence intensity for HFST was not high enough to eliminate all instantaneous reverse flow in the vicinity of the wall, its effect was strong enough to maintain a positive mean velocity near the wall and hence to maintain a positive mean velocity gradient and positive skin friction throughout. An increased free-stream turbulence level thus leads to mean velocity profiles with a lower value of the form parameter H_{12} while the pressure distribution and the Reynolds number remain approximately the same. This is an interesting variation of the suggestion made by Clauser 1954 (see also Rotta 1962) that two boundary layers in the same pressure distribution can have widely different velocity profiles. It should also be noted that the effect of the FST on the mean velocity profile and the skin friction is much stronger in an adverse pressure gradient than in a zero pressure gradient. Another effect of the FST is to decrease the flatness factor F_u at the boundary layer edge.

The profiles of the four Reynolds stresses in the upstream region of the test boundary layer (figure 13) show for HFST higher peak values with a characteristic hump in the $\overline{u'^2}$-profile. This higher level continues in the downstream direction for $\overline{u'^2}$ and $\overline{w'^2}$ (figure 17) and less so for $\overline{v'^2}$ and $\overline{u'v'}$ (figure 18), emphasizing the important role of the streamwise fluctuating component (see also Hancock & Bradshaw (1989)). For HFST the profiles of the production term in the Reynolds stress transport equation exhibit smaller peaks in the outer layer due to the reduced mean velocity gradient (figures 19*a*, *b* and 20*a*, *b*) and an increase near the wall where the mean velocity gradient $\partial\overline{u}/\partial\overline{y}$ is increased.

The diffusion due to the normal fluctuating velocity v' is little changed by FST (figure 21) but, since the pressure fluctuation field generated by the FST is probably increased, the pressure–velocity correlation term should further the diffusion process.

It has not been possible in this experiment to distinguish between free-stream and boundary layer fluid in order to facilitate investigations of the entrainment mechanism changed by FST. In 'conventional' boundary layers this has been done by introducing, for example, a passive scalar such as heat and determining zonal contributions by conditional sampling and hot–cold discrimination (Hancock & Bradshaw (1989)). It is not clear to us, however, how to adapt this technique to flows with reverse-flow regions.

In qualitative agreement with the experiment of AF and the numerical computation of Na & Moin 1998 there is a region of instantaneous reverse flow half a bubble length upstream of the mean separation line and a full bubble length downstream of mean reattachment. This is the fetch within which buffeting is taking place. Mean separation and reattachment lines are characterized by $\tau_w = 0$ and $\chi_w = 50\%$ with velocity profiles having a form parameter H_{12} with a value of about 3 and little dependent on FST. In all cases the bubble was well definded and repeatable from day to day.

In the separation region the fluctuating skin friction τ'_w and its higher moment F_{τ_w} change very little for LFST and HFST showing only a small effect of FST. The fall of

τ'_w indicates that the amount of turbulence on the wall decreases through separation (AF) and the high values of F_{τ_w} suggest that the interaction of low- and high-speed fluid is strong and remains so throughout the redevelopment region. The skewness S_{τ_w} remains close to 1 for HFST as in a canonical boundary layer.

The 'boundary layers' downstream of the reverse-flow region were subject to three different initial conditions: two mean reverse-flow regions of different length and height and an 'embedded' instantaneous reverse-flow region ($\chi_{max} \approx 12\%$). Our data add further proof to the rather astonishing result that the developing flow is qualitatively independent of the upstream disturbance if the latter is overwhelming in the sense of Bradshaw & Wong (1972); the layer, however, remains in a different state from that of a canonical ZPG boundary layer. AF found that the slow response of the Reynolds stresses near the wall is an unusual and important feature of this flow and, one may add now, this is also true when FST is present. Turbulence measurements show that the $\overline{v'^2}$ and $\overline{u'v'}$ distributions have very small values in the inner region of the boundary layer in agreement with small production terms and practically non-existent turbulent diffusion. These features are confirmed by the structure parameter a_1 which indicates a lack of near-wall organized structure compared with a canonical boundary layer (see also AF). For cases LFST and HFST only the streamwise Reynolds normal stress component $\overline{u'^2}$ shows a gradual formation of a near-wall peak at the last downstream station but far below the peak value in a canonical boundary layer. In any case the mean velocity profile develops its canonical form – the log-law distribution – in the inner region faster than the turbulence quantities.

In the outer region of the boundary layer the wake part of the mean velocity profile is still underdeveloped and in accordance with Castro & Epik (1998) we find that the FST level of the outer flow ($Tu_\delta \leqslant 7\%$) hardly changes the redevelopment process of the boundary layer. Downstream of an 'overwhelming' disturbance, formed by mean and instantaneous reverse-flow regions, the redeveloping boundary layer appears to have outer-layer structure with relatively little inner-layer structure (AF) and this configuration prevents the internal-layer response mechanism which is usually found in relaxing boundary layers and which would typically be expected to re-energize the inner layer. A possible approach towards an understanding of this phenomenon might lie along the lines suggested by Hunt & Durbin (1999) to investigate the interaction between an external vortical flow containing perturbations and a largely shielded inner region of a boundary layer.

We can confirm the finding of Thole & Bogard (1996) in that FST leads to a larger inertial subrange and a broadening of the spectra (but only in the high wavenumber region) as compared with the LFST case, but we did not find a dominance of the FST in the near-wall region. This might be due to the lower turbulence levels in our investigation as well as to the relatively small FST length scales compared to those of Thole & Bogard (1996), so that the spectral characteristics of the FST are difficult to distinguish from the boundary layer spectra.

M. K. gratefully acknowledges the financial support by DFG for the research project Fe 43/38-1 to 5.

REFERENCES

Alving, A. E. & Fernholz, H. H. 1995 Mean velocity scaling in and around a mild, turbulent separation bubble. *Phys. Fluids* **7**, 1956–1969 (referred to herein as AF).

Alving, A. E. & Fernholz, H. H. 1996 Turbulence measurements around a mild separation bubble and downstream of reattachment. *J. Fluid Mech.* **322**, 297–328.

Baines, W. D. & Peterson, E. G. 1951 An investigation of flow through screens. *Trans. ASME* **73**, 467–480.

Bearman, P. W. & Morel, T. 1983 Effect of free stream turbulence on the flow around bluff bodies. *Prog. Aerospace Sci.* **20**, 97–123.

Blair, M. F. 1983 Influence of free-stream turbulence on turbulent boundary layer heat transfer and mean profile development. *Trans. ASME* C: *J. Heat Transfer* **105**, 33–40 and 41–47.

Bradbury, L. J. S. & Castro, I. P. 1971 A pulsed–wire technique for velocity measurements in highly turbulent flow. *J. Fluid Mech.* **22**, 679–687.

Bradshaw, P. & Wong, F. Y. F. 1972 The reattachment and relaxation of a turbulent shear layer. *J. Fluid Mech.* **52**, Part 1, 113–135.

Castro, I. P. 1984 Effects of free-stream turbulence on low reynolds number boundary layers. *Trans. ASME* I: *J. Fluids Engng* **106**, 298–306.

Castro, I. P. 1990 On separated shear layers. *1988 Z. Zariç Memorial Conf.* (ed. S. J. Kline & N. H. Afgan) pp. 123–38. Hemisphere.

Castro, I. P. 1992 Pulsed-wire anemometry. *Expl Therm. Fluid Sci.* **5**, 770–780.

Castro, I. P. & Epik, E. 1996 Boundary-layer relaxation after a separated region. *Expl Thermal Fluid Sci.* **13**, 338–348.

Castro, I. P. & Epik, E. 1998 Boundary layer development after a separated region. *J. Fluid Mech.* **374**, 91–116.

Castro, I. P. & Haque, A. 1988 The structure of a shear layer bounding a separtion region. Part 2. Effects of free-stream turbulence. *J. Fluid Mech.* **192**, 577–595.

Clauser, F. H. 1954 Turbulent boundary layers in adverse pressure gradients. *J. Aero. Sci.* **21**, 91–108.

Dengel, P. 1992 Über die Struktur und die Sensibilität einer inkompressiblen turbulenten Grenzschicht am Rande der Ablösung. Dissertation, Hermann-Föttinger-Institut der TU-Berlin.

Dengel, P. & Fernholz, H. H. 1990 An experimental investigation of an incompressible turbulent boundary layer in the vicinity of separation. *J. Fluid Mech.* **212**, 615–636 (referred to herein as DF).

Driver, D. M. 1991 Reynolds shear stress measurements in a separated boundary layer flow. *AIAA Paper* 91–1787.

Erm, L. P. 1988 Low Reynolds-number turbulent boundary layers. PhD thesis, University of Melbourne.

Fernholz, H. H. 1993 Management and control of turbulent shear flows. *Z. Angew. Math. Mech.* **73**, 287–300.

Fernholz, H. H. 1994 Near–wall phenomena in turbulent separated flows. *Acta Mechanica* **4**, suppl 4: 57–67.

Fernholz, H. H. & Finley, P. J. 1996 The incompressible zero–pressure–gradient turbulent boundary layer: An assessment of the data. *Progr. Aerospace Sci.* **32**, 245–311.

Fernholz, H. H., Janke, G., Schober, M., Wagner, P. M. & Warnack, D. 1996 New developments and applications of skin–friction measuring techniques. *Meas. Sci. Technol.* **7**, 1396–1409.

Hancock, P. E. 1980 The effect of free-stream turbulence on turbulent boundary layers. PhD thesis, Imperial College London.

Hancock, P. E. & Bradshaw, P. 1983 The effect of free-stream turbulence on turbulent boundary layers. *Trans. ASME* I: *J. Fluids Engng* **105**, 284–289.

Hancock, P. E. & Bradshaw, P. 1989 Turbulence structure of a boundary layer beneath a turbulent free stream. *J. Fluid Mech.* **205**, 45–76.

Hillier, R. & Cherry, N. J. 1981 The effects of stream turbulence on separation bubbles. *J. Wind Engng Ind. Aerodyn.* **8**, 49–58.

Hinze, J. O. 1975 *Turbulence*, 2nd Edn.: McGraw-Hill.

Hoffmann, J. A. 1981 Effects of free-stream turbulence on diffuser performance. *Trans. ASME* I: *J. Fluids Engng* **103**, 385–390.

Hoffmann, J. A. & Kassir, S. M. 1988 Effects of free-stream turbulence on turbulent boundary layers with mild adverse pressure gradients. *ASME 88-3757-CP.*

Hunt, J. C. R. & Durbin, P. A. 1999 Perturbed vortical layers and shear sheltering. *Fluid Dyn. Res.* **24**, 375–404.

Isomoto, K. & Honami, S. 1989 The effect of inlet turbulence intensity on the reattachment process over a backward facing step. *Trans. ASME* I: *J. Fluids Engng* **111**, 87–92.

KALTER, M. 2001 Beeinflussung einer stark gestörten Grenzschicht mit Druckanstieg durch die Turbulenzstruktur der Außenströmung. Dissertation TU Berlin D 83 (in progress).

KALTER, M. & FERNHOLZ, H. H. 1995 The influence of free–stream turbulence on an axisymmetric turbulent boundary layer in, and relaxing from, an adverse pressure gradient. *Advances in Turbulence* V (ed. R. Benzi), pp. 261–265. Kluwer.

KISTLER, A. L. & VREBALOVICH, T. 1966 Grid turbulence at large Reynolds numbers. *J. Fluid Mech.* **26**, 37–47.

KIYA, M. & SASAKI, K. 1983 Free-stream turbulence effects on a separation bubble. *J. Wind Engng Ind. Aerodyn.* **14**, 375–386.

MURLIS, J., TSAI, H. M. & BRADSHAW, P. 1982 The structure of turbulent boundary layers at low Reynolds numbers. *J. Fluid Mech.* **122**, 13–56.

NA, Y. & MOIN, P. 1998 Direct numerical simulation of a separated turbulent boundary layer. *J. Fluid Mech.* **374**, 379–405.

PATEL, V. C. 1965 Calibration of the Preston tube & limitations on its use in pressure gradients. *J. Fluid Mech.* **23**, 185–208.

PRESS, W. H., FLANNERY, B. P., TEUKOLSKY, S. A. & VETTERLING, W. T. 1988 *Numerical Recipes in C*. Cambridge University Press.

ROTTA, J. C. 1962 Turbulent boundary layers in incompressible flow. *Prog. Aeronaut. Sci.* **II**, 1–220.

ROTTA, J. C. 1972 *Turbulente Strömungen*. B. G. Teubner, Stuttgart.

RUDERICH, R. & FERNHOLZ, H. H. 1986 An experimental investigation of a turbulent shear flow with separation, reverse flow and reattachment. *J. Fluid Mech.* **163**, 283–322.

SCHATZ, M., RUNG, T. & THIELE, F. 1998 Computational modelling of the influence of free-stream turbulence on boundary layer flows complex boundary–layer flows. *Proc. 3rd Intl Conf. Fluid Mech.*, Beijing Inst. of Technology Press.

SENDSTADT, P. R. & MOIN, P. 1992 The near-wall mechanics of three-dimensional turbulent boundary layers. *Thermosci. Div. Stanford Univ. USA, Rep.* TF-57.

SIMPSON, R. L. 1981 A review of some phenomena in turbulent flow separation. *Trans. ASME* I: *J. Fluids Engng* **103**, 520–533.

SIMPSON, R. L. 1989 Turbulent boundary layer separation. *Ann. Rev. Fluid Mech.* **21**, 205–234.

SIMPSON, R. L., AGARWAL, N. K., NAGABUSHANA, K. A. & OLÇMEN, S. 1990 Spectral measurements and other features of separating turbulent flows. *AIAA J.* **28**, 446–452.

SIMPSON, R. L., CHEW, Y. T. & SHIVAPRASAD, B. G. 1981 The structure of a separating turbulent boundary layer. Part 1. Mean flow and Reynolds stresses. *J. Fluid Mech.* **113**, 23–51.

SIMPSON, R. L., STRICKLAND, J. H. & BARR, P. W. 1977 Features of a separating turbulent boundary layer in the vicinity of separation. *J. Fluid Mech.* **79**, 553–594.

SMITS, A. J. & WOOD, D. H. 1985 The response of turbulent boundary layers to sudden perturbations. *Ann. Rev. Fluid Mech.* **17**, 321–358.

SPALART, P. R. 1988 Direct simulation of a turbulent boundary layer up to Re_θ =1410. *NASA TM* 89407; *J. Fluid Mech.* **187**, 61–98.

STEVENSON, W. H., THOMSON, H. D. & CRAIG, R. R. 1984 Laser velocimeter measurements in highly turbulent recirculating flows. *Trans. ASME* I: *J. Fluids Engng* **106**, 173–180.

THOLE, K. A. & BOGARD, D. G. 1996 High freestream turbulence effects on turbulent boundary layers. *Trans. ASME* I: *J. Fluids Engng* **118**, 276–284.

WAGNER, P. M. 1986 Entwicklung eines verbesserten Pulsdrahtanemometers zur Erfassung von Geschwindigkeiten und Korrelationen in turbulenten Strömungen. Diplomarbeit, Hermann-Föttinger-Institut der TU-Berlin.

WAGNER, P. M. 1995 Kohärente Strukturen der Turbulenz im wandnahen Bereich von Ablösegebieten. Dissertation, TU Berlin Verlag Dr. Köster, Berlin.